



HAL
open science

4D forward stratigraphic modelling of the Late Quaternary Congo deep-sea fan : Role of climate/vegetation coupling in architectural

Dimitri Laurent, Tania Marsset, Laurence Droz, Didier Granjeon, Stéphane Molliex, Marie Picot, Marina Rabineau

► To cite this version:

Dimitri Laurent, Tania Marsset, Laurence Droz, Didier Granjeon, Stéphane Molliex, et al.. 4D forward stratigraphic modelling of the Late Quaternary Congo deep-sea fan : Role of climate/vegetation coupling in architectural. *Marine Geology*, 2020, 429, pp.106334. 10.1016/j.margeo.2020.106334 . hal-02973284

HAL Id: hal-02973284

<https://ifp.hal.science/hal-02973284>

Submitted on 21 Oct 2020

HAL is a multi-disciplinary open access archive for the deposit and dissemination of scientific research documents, whether they are published or not. The documents may come from teaching and research institutions in France or abroad, or from public or private research centers.

L'archive ouverte pluridisciplinaire **HAL**, est destinée au dépôt et à la diffusion de documents scientifiques de niveau recherche, publiés ou non, émanant des établissements d'enseignement et de recherche français ou étrangers, des laboratoires publics ou privés.

4D forward stratigraphic modelling of the Late Quaternary Congo deep-sea fan: Role of climate/vegetation coupling in architectural evolution

Abstract

The relative impacts of autogenic and allogenic controls on the architectural evolution of deep-sea fans are not well constrained, mainly because of the difficulty in evaluating the role of each control on any specific stratigraphic pattern. This study presents four-dimensional (4D) forward stratigraphic modelling of the Late Quaternary Congo Axial Fan, which provides new insights on forcing factors of sedimentation over time. This modelling is based on a geological model describing successive sedimentary progradational/retrogradational cycles in the Congo turbidite system during the last 38 kyr. Analyses of geophysical and marine core data have suggested that the architectural cycles were controlled by changes in fluvial sediment discharge in relation to arid and humid periods in the Congo River watershed. The aims of this study were to simulate the architectural evolution of the Late Quaternary Congo Axial Fan from 210 ka to the present and investigate the factors controlling sedimentation using DionisosFlowTM, a process-based stratigraphic forward modelling software. For this objective, several scenarios were tested to simulate the role of autogenic and climate forcings based on proxies recorded in marine sediments. The modelling results confirmed that climatic variations of sediment and water discharge succeeded in reproducing the timing, position, and sediment volume of basin-scale prograding/retrograding cycles. The best-fit simulations particularly emphasise the role of continental vegetation cover expansion, governed by the precession-driven West African monsoon, on the sediment flux to the deep-marine environment. This vegetation/climate coupling acts directly on the transport capacity of flow over time by controlling the magnitude of river runoff and the timing of sediment production, storage, and transfer from the continent to the ocean. Thus, our results confirm the utility of stratigraphic forward models in constraining ‘source-to-sink’ models for the architectural evolution of submarine fans.

Keywords: Congo; Quaternary; turbidite system; deep-sea fan; vegetation/climate coupling; sedimentary cycles; geophysical data; stratigraphic modelling; DionisosFlowTM; palaeoclimate

32 **1. Introduction**

33 A large number of interacting autogenic (internal) and allogenic (external) factors influence
34 the evolution of submarine fans, the largest depositional bodies on the planet. Crucial control in the
35 position and timing of avulsions (abandonment and lateral migration of channels) along turbidite
36 systems is associated with internal factors such as topographic compensation, sinuosity of channels,
37 and the dynamics of currents, which favour instabilities within the channel and levee systems and
38 emplacement of mass transport complexes (Flood and Piper, 1997; Pirmez et al., 1997; Lopez, 2001;
39 Kneller, 2003; Maslin et al., 2006; Kolla, 2007; Labourdette and Bez, 2010; Armitage et al., 2012).
40 In addition, several external factors affecting sedimentation in turbidite systems have also been
41 outlined, such as eustacy (Posamentier et al., 1991; Lopez, 2001; Posamentier and Kolla, 2003;
42 Bourget et al., 2011), intra-basinal and extra-basinal tectonic movements (Hoorn et al., 1995;
43 Prather et al., 1998; Turakiewicz, 2004; Anka et al., 2009; Broucke et al., 2004; Sømme et al., 2009;
44 Prather, 2020), and climate changes in the drainage basin (e.g. Milliman and Syvitski, 1992; Zabel
45 et al., 2001; Toucanne et al., 2008; Toucanne et al., 2012; Ducassou et al., 2009; Picot et al., 2019),
46 which are sometimes linked to orbital periodicities (Foucault et al., 1987; Weltje and de Boer, 1993;
47 Schneider et al., 1997; Weber et al., 2003; Heard et al., 2008; Ducassou et al., 2009; Cantalejo and
48 Pickering, 2015; Scotchman et al., 2015). In particular, several authors have highlighted the role of
49 Milankovitch precession cycles in the variation of monsoon intensity, which inevitably impacts the
50 sediment yield in drainage basins and thus the sediment transfer from rivers to deep-sea fans
51 (Bengal Fan – Weber et al., 2003; Nile system – Ducassou et al., 2009; Niger Delta – Zabel et al.,
52 2001; Congo Fan – Schneider et al., 1997; Holtvoeth et al., 2001; Caley et al., 2011; Picot et al.,
53 2019). It is now accepted that the impact of climate changes on the sediment budget must be studied
54 from the perspective of climate/vegetation coupling (Foley et al., 1994; Kutzbach et al., 1996;
55 Brovkin et al., 1998; Ganopolski et al., 1998; Claussen et al., 1999), as the extent and density of
56 vegetation partly control sediment production on land through the balance between mechanical and

57 chemical weathering of soils (e.g. Renard et al., 1997). However, if the link between
58 climate/vegetation coupling and sediment transfer to the ocean is inferred from proxies in marine
59 sediment cores, the response in terms of the architectural evolution of the submarine fan is not well
60 constrained. More specifically, the respective roles of the climate-driven variations of water
61 discharge and sediment flux cannot be investigated without individualising the factors responsible
62 for specific stratigraphic architecture in deep-marine basins, both in time and space. With this
63 objective, recent studies have moved toward forward modelling; more specifically, slope- and
64 water-driven diffusion process-based simulations have already shown their usefulness in
65 investigating sedimentary transfers in continental shelf and deep-water systems using short
66 computation times (Kaufman et al., 1991; Granjeon and Joseph, 1999; Steckler et al., 1999;
67 Rabineau et al., 2005; Lai and Capart, 2007; Mitchell and Huthnance, 2008; Alzaga-Ruiz et al.,
68 2009; Csato et al., 2013; Seard et al., 2013; Gvirtzman et al., 2014; Leroux et al., 2014; Deville et
69 al., 2015). However, investigations of the architecture of turbidite systems on abyssal plains using
70 diffusion models at a ‘source-to-sink’ scale are very recent (Deville et al., 2015; Hawie et al., 2018;
71 Burgess et al., 2019; Hawie et al., 2019; Sangster et al., 2019) and need to be enriched and
72 confirmed by additional studies.

73 In this sense, the Late Quaternary Congo Fan is a good candidate to test diffusion process-
74 based models as the large geophysical and geological database available for this fan may help to
75 constrain the potential effects of continental climatic changes on the growth patterns of the fan over
76 time. This fan was the subject of nine oceanographic cruises between 1992 and 2011, led by Ifremer
77 and the University of Brest in collaboration with Total, with a total acquisition of 16,000 km of
78 seismic lines, chirp sonar bottom profiles, multi-beam bathymetric lines, and 172 marine cores.
79 Analysis of this database revealed successive progradational/retrogradational cycles of depocentres
80 over time since at least 210 ka (Picot et al., 2016). Picot et al. (2019) demonstrated that the growth
81 pattern of the fan since 38 ka is potentially linked to changes in water and sediment discharge to the

82 ocean in relation to the timing of variations of monsoon intensity. Beyond 38 ka and up to 210 ka,
83 there are some uncertainties in the chronostratigraphic calibration, partly because of incomplete
84 geophysical coverage and inherent difficulties in accurately dating sediments in turbiditic
85 environments. If the variation in monsoon intensity controlled the sediment supply over time for the
86 last 38 kyr, other mechanisms may be involved at longer time scales. This work constitutes the first
87 attempt to model the three-dimensional (3D) architectural evolution of the Late Quaternary Congo
88 Fan using DionisosFlowTM, a process-based diffusion forward stratigraphic model (Granjeon, 1997;
89 Granjeon and Joseph, 1999). The main objective of this study was to demonstrate the possible
90 correspondence between the stratigraphic architecture of a deep-sea fan produced using diffusion-
91 based stratigraphic forward modelling software and a real-world case study through an inversion
92 process. Our method is based on: (i) determination of the simulation inputs inferred from the
93 seismic and geological data, and demonstration of the relevance of the slope- and water-driven
94 diffusion model to simulate the turbidite environment, and (ii) validation of the model against
95 recent geological mapping and the conceptual model proposed by Picot et al. (2019) to identify the
96 relative impacts of internal and external factors on sediment transport and distribution in the
97 turbidite environment. This study helps to build confidence in the use of diffusion process-based
98 stratigraphic forward models for construction of static economic reservoirs (for energy, storage, etc.)
99 and understanding the distribution of terrestrial pollutants (e.g. microplastics; Kane et al., 2019)
100 conveyed by rivers to the ocean.

101

102

103 **2. The Congo sedimentary system**

104 **2.1. The Congo River**

105 The Congo Fan is located on the Congo–Angola margin (Fig. 1). Its formation was initiated
106 just after a major submarine erosion event that occurred on the outer shelf during the Early

107 Oligocene (Nze Abeigne, 1997; Lavier et al., 2000; Lavier et al., 2001). At this time, a combination
108 of continental uplift, associated global sea-level fall, and the establishment of a humid climate in the
109 Congo River watershed led to a considerable increase in sediment supply to the Atlantic Ocean
110 (Droz et al., 1996; Anka and Séranne, 2004). The low degree of crystallinity of smectite confirms
111 that at least 95% of the deposited sediment in the submarine fan is supplied by the Congo River,
112 and that a negligible component may be associated with oceanic currents or trade winds (Gingele et
113 al., 1998). The Congo River is currently one of the largest river systems in the world, with a length
114 of 4,370 km draining a catchment area of 3.7×10^6 km² (Van Weering and Van Iperen, 1984). The
115 Congo River watershed receives $5,530 \times 10^9$ m³ of rainfall annually, of which $1,350 \times 10^9$ m³ was
116 estimated by Moguedet (1988) to feed the ocean, representing 80% of the fluvial supply in the Gulf
117 of Guinea and 4% of the world's carbon input to the ocean (Martins and Probst, 1991; Rabouille et
118 al., 2019). At present, its average flow of 41,000 m³/s (Laraque et al., 1993; Laraque et al., 2009;
119 Laraque et al., 2013; Alsdorf et al., 2016) ranks the Congo River second to the Amazon River
120 globally. The sediment flux is comparatively low (ranked 17th worldwide) with a mean value of 86
121 Mt/yr (Fig. 1), including 33 Mt/yr of total suspended sediments and 53 Mt/yr of total dissolved
122 matter (Laraque et al., 2009, 2013). This weak sediment load is probably related to the present
123 climate of West Africa, where chemical erosion and vegetation cover are widespread because of
124 warm and humid conditions, even though mechanical erosion still prevails (Summerfield and
125 Hulton, 1994; Gaillardet et al., 1995). The low mean slope gradient of the Congo River watershed
126 has led to the formation of several lakes and pools, which favour trapping of coarse-grained
127 materials in the central part of the basin (Molliex et al., 2019) and in the estuary in the form of
128 prograding sandy river mouth bars (Moguedet, 1988; Wefer et al., 1998). Nevertheless, the real
129 proportion of sediment reaching the submarine canyon remains unknown. It is assumed that
130 between one-third and two-thirds of the sediment supply conveyed by the river currently reaches the

131 oceanic domain (Moguedet, 1988), but the lack of direct measurements in the estuary does not
132 allow confirmation of this proportion.

133

134

135

136 **2.2. General architecture of the Late Quaternary Congo Fan since 210 ka**

137 The Late Quaternary Congo Fan can be divided into three main entities; from oldest to
138 youngest, these are—the Northern Fan (780 to 540 ka), the Southern Fan (540 to 210 ka), and the
139 Axial Fan (210 ka to present) (Droz et al., 2003). Extensive geophysical surveys carried out from
140 1992 to 2011 (see the legend of Fig. 1 for references to cruises) provided an accurate map of the
141 Late Quaternary Congo turbidite system (Fig. 2a). An integrated analysis of architectural
142 parameters (channel length and distance of avulsion points from the source point) of the Congo Fan
143 revealed organisation into prograding/retrograding architectural cycles (Fig. 2b) (Marsset et al.,
144 2009; Picot et al., 2016). The cycles belonging to the Axial Fan were placed into an accurate
145 chronostratigraphic framework based on sediment dating (Picot et al., 2019)—cycle A from 210 to
146 130–110 ka, cycle B from 130–110 to 80–70 ka, cycle C from 80–70 to 11 ka, and cycle D, which
147 is still active, from 11 ka to the present. The entire volume of the Axial Fan has been evaluated to
148 be 7,500 km³ (this study).

149

150 **2.3. Conceptual model of Congo Fan architecture since 38 ka**

151 According to Picot et al. (2016), the architectural evolution of the Axial Fan shows that
152 internal control by topographic compensation is omnipresent and linked to the local slope gradient
153 and inherited geometries of the previous deposits (Northern and Southern fans). This is particularly
154 the case for middle-fan and down-fan avulsions, which are more easily developed because of
155 limited confinement of the turbidity currents in the distal parts of the basin. However, the

156 occurrence of very up-fan avulsion before the complete infill of the available space down-fan
157 (accommodation) suggests another external control on sedimentation (Picot et al., 2016). Eustatic
158 control is rejected as the Congo Fan is a perennial system with a permanent connection between the
159 Congo River and the canyon head, which penetrates 30 km inside the estuary, regardless of sea-
160 level variations from 210 ka to the present (Heezen et al., 1964; Van Weering and Van Iperen, 1984;
161 Mogueudet, 1988; Droz et al., 1996; Savoye et al., 2000; Babonneau, 2002; Savoye et al., 2009;
162 Picot et al., 2019). The impact of continental uplift since the Pliocene on the morphology of the
163 Congo River watershed, and thus on sediment production and flux, is not well constrained and may
164 even be non-existent, as suggested by the study of Lavier et al. (2001). In contrast, the role of
165 climate on sedimentation in the Congo Fan is well evidenced by multi-proxy studies on the marine
166 reference core KZai-02 (see Fig. 1 for location and Fig. 2b), which specifically highlight the link
167 between sediment flux and palaeoclimatic signals (Gingele et al., 1998; Molliex et al., 2019; Picot
168 et al., 2019). During the last 210 kyr, the Congo River watershed has been characterised by a
169 succession of humid and arid periods corresponding respectively to interglacial and glacial or
170 highstand and lowstand periods (Schneider et al., 1997; Jahns, 1996; Gingele et al., 1998; Dalibard
171 et al., 2014). The glacial/lowstand episodes (Marine Isotope Stages [MIS] 6, 4, and 2) were
172 characterised by an arid climate synchronous with the development of icecaps at the poles
173 (deMenocal et al., 1993; Leroux, 1993), whereas the interglacial/highstand stages (MIS 7, 5, 3, and
174 1) were wetter (Schneider et al., 1997; Dupont et al., 2000) and associated with strengthening of the
175 West African monsoon regime (Gingele et al., 1998). In particular, the sediment supply to the ocean
176 has been correlated with 23-kyr precession cycles (Fig. 2), which govern the intensity of the West
177 African monsoon (Schneider et al., 1997; Gingele et al., 1998; Caley et al., 2011). Picot et al. (2019)
178 confirmed that for the last 38 kyr, the primary control of sedimentation has been monsoon-driven
179 climatic changes acting on the liquid and solid fluvial discharges and thus on turbidity current
180 capacity (Fig. 3). The progradation of the system is correlated with humid periods with elevated

181 transport capacity of turbidity currents. This is because a high-intensity monsoon increases fluvial
182 discharge and chemical erosion, which put fine-grained material into suspension, thus leading to a
183 muddy sediment supply in the turbidite environment. In contrast, retrogradation of depocentres
184 occurred during arid periods. These periods were characterised by low intensity of rainfall, limited
185 runoff, and considerable predominance of mechanical erosion associated with limited vegetation
186 cover on land, thus leading to a decrease in the transport capacity of turbidity currents. Finally,
187 arid/humid transition periods were conducive to major retrogradation and up-fan avulsion followed
188 by new increases of the transport capacity of turbidity currents, which resulted from the onset of
189 precipitation when vegetation cover had not yet colonised the watershed.

190

191

192 **3. Data and methods**

193 **3.1. DionisosFlowTM, a four-dimensional forward stratigraphic model**

194 Based on our objectives, dynamic deterministic modelling was selected as the most
195 appropriate tool because its physical laws of sediment transport lead to the simulation of average
196 sedimentary architecture and facies distribution over time (e.g. Granjeon, 1997). We used the
197 DionisosFlowTM software, which allows simulation of sediment transport and 3D geometric
198 reproduction of sedimentary units from deltaic to deep-sea environments, based on physical
199 processes such as sea-level changes, tectonics, and sediment supply and transport (Granjeon, 1997;
200 Granjeon and Joseph, 1999) (Fig. 4). At each time step, the software quantifies the accommodation
201 (according to basin geometry, subsidence history, and sea-level variation) and sediment supply
202 based on large-scale transport laws (Granjeon, 1997; Granjeon and Joseph, 1999). Two main types
203 of transport mechanisms are defined in the simulation: (i) long-term transport such as water-driven
204 and slope-driven transport and (ii) short-term transport such as debris flows (Granjeon and Joseph,
205 1999). The transport of particles is governed by a diffusion law, coupled with a continuity equation

206 for sediment mass conservation, which expresses the sediment flux as a function of slope gradient,
207 water discharge, and diffusion coefficients:

$$208 \quad Q_{s,i} = v_i * (K_{s,i} + K_{w,i} * Q_w^m) * \Delta h^n, \quad (1)$$

209 where $Q_{s,i}$ is the flux of the i th granulometric class (km^2/yr); v_i the proportion of the i th sediment
210 class in the sediment flow; $K_{s,i}$ and $K_{w,i}$ are the diffusion coefficients for slope-driven transport
211 (mainly slow creep) and water-driven processes, respectively (km^2/yr), reflecting the transport
212 efficiency in both the marine and continental domains; Q_w is the dimensionless local water
213 discharge; Δh is the local gradient of the basin slope; and m and n are constants (usually between 1
214 and 2) defining a nonlinear equation that reflects the balance between slope- and water-driven
215 transport. Coupling with the mass balance equation allows quantification of the erosion and
216 sedimentation rates of each granulometric class in each cell of the model, and thus the calculation of
217 volumes of deposited sediment. This diffusion process-based software is applicable at a resolution
218 corresponding to a large time scale, from kyr to several Myr, and at the sedimentary basin-scale,
219 from several tens to several hundreds of km^2 . The slope reflects the driving force resulting from the
220 complete conversion of potential energy in kinetic energy (e.g. Paola et al., 1992). Processes that
221 are not associated with water- or slope-driven transport, such as aeolian processes and oceanic
222 currents, are not simulated. Moreover, as the purpose of DionisosFlowTM is to determine the
223 average geometry and facies distribution inside a stratigraphic unit at a given time step, it is likely
224 infeasible to model one-time events (such as floods and storms) and individual flows in the deep-
225 sea environment. Therefore, density-stratified turbidity current flow, as observed in nature, cannot
226 be simulated through the diffusion approach, and some important processes, such as external levee
227 development by flow stripping and overspilling, are not modelled. Consequently, only large-scale
228 and long-term evolution of the turbidite system can be modelled with this method, which fits well
229 with our objective of recreating the successive periods of progradation and retrogradation of
230 sedimentary units identified in the Late Quaternary Congo Fan by Picot et al. (2016, 2019).

231 A climate module is integrated in the software, providing the possibility to construct curves
232 of Q_s and Q_w over time by defining the pattern (such as sinusoidal and sawtooth) and the period of
233 the curve. In addition, the software integrates a module named HEST based on hydrological
234 statistics calculated for five major rivers in the United States (the Eel, Colorado, Mississippi,
235 Hudson, and Delaware rivers). This module allows the simulation of both Q_s and Q_w during high-
236 and low-energy events based on their respective durations as well as their relative contributions in
237 terms of sediment supply.

238 The software CougarFlowTM (OpenFlow Suite) finalises the model calibration by
239 considering the impact of the uncertainties of the input parameters on the simulation results (Fig. 4).
240 This module provides the opportunity to launch a ‘multi-realisation simulation’ to test the effects of
241 the variations of the input parameters in response surface modelling (RSM, e.g. Gervais et al., 2017;
242 Hawie et al., 2019; Sangster et al., 2019). Then, Monte-Carlo sampling of the RSM can be
243 performed to determine a probabilistic distribution of the responses of the models.

244

245 **3.2. Strategy and calibration of simulations**

246 In process-based stratigraphic modelling, the stratigraphic organisation of deposits is a
247 function of the temporal evolution of three main parameters—(i) accommodation, (ii) sediment
248 supply from one or several sources at the boundary of the initial grid, and (iii) sediment transport.
249 At the end of the simulation, a large panel of output data is available, such as the thickness of the
250 deposit (and thus its volume), the distribution of sedimentary facies, the evolution of water
251 discharge along the sedimentary system, and the sedimentation rate (Fig. 4).

252 In our study, the calibration of the model after simulation was mainly based on the
253 architectural parameters defined by Picot et al. (2016) and the deposited sediment volume of each
254 prograding/retrograding cycle inferred from seismic data and computed with the Kingdom Suite
255 software (see Picot et al. (2016) for a complete description of the seismic data used to establish the

256 architecture of the fan). Isopach maps were constructed after simulations for each architectural
257 cycle, and the sedimentary volumes of compacted sediments were calculated for comparison with
258 the Axial Fan.

259 The next step was uncertainty analysis of the models using CougarFlowTM. Latin hypercube
260 sampling RSM was used to run 100 simulations of the maximum and minimum values of inputs to
261 predict the responses of the models in terms of sedimentary deposit volumes over time. Then,
262 Monte-Carlo sampling of the RSM was performed to compare the simulated deposit volumes with
263 those calculated for the Axial Fan based on seismic interpretation.

264

265 **3.3. Model setup**

266 The diffusion process-based approach means that sedimentary processes of transport and
267 deposition are averaged over a given period of time. For all our simulations, the time step was set at
268 5 kyr to test orbital cycles (with a minimum scale of 23 kyr). The model size extended from
269 Brazzaville in the Congo watershed to the deep-sea environment for a total length of 1,383 km and
270 a width of 468 km (Fig. 5). The cell size was fixed at $6 \times 6 \text{ km}^2$, corresponding to the minimum
271 space between two-dimensional (2D) seismic lines. The model boundaries were closed for sediment
272 transport, meaning that all the sediments were deposited inside the defined model size. Closing the
273 model boundaries allowed us to highlight sediment transport inconsistencies regarding the sediment
274 distribution in the real Axial Fan, particularly laterally to the fan axis where the depocentres are
275 well delimited by geophysical cover (Fig. 2).

276 As mentioned above, during simulation, sedimentary particles were transported and
277 deposited according to three main input parameters (Granjeon et al., 1994):

278 (i) *Accommodation (basin morphology, subsidence, and eustacy)*: Because of the short
279 simulated time interval, we assumed that accommodation was mainly controlled by flexure and sea-
280 level variation. To define the initial bathymetry of the basin at the starting age of the simulation, we

281 used the base of the Axial Fan interpreted from seismic data and corrected it based on the flexural
282 deformation linked to the sediment load of the overlying turbiditic deposits according to the
283 calculation methods used by Nygård et al. (2004). The high-resolution LR04 $\delta^{18}\text{O}$ curve of Lisiecki
284 and Raymo (2005) and interpreted sea-level variation of Spratt and Lisiecki (2016) were chosen
285 (Fig. 2b) to define eustacy in all simulations. No tectonic subsidence was indicated in the
286 simulations because of the absence of tectonic movement in the margin and deep-sea basin during
287 the last 210 kyr (Lavie et al., 2001).

288 *(ii) Sediment transport (water discharge, lithology, and diffusion coefficient):* We
289 assumed that the fluvial discharge in the Congo River ran basinward as gravitational flows
290 according to hyperpycnal transport or slope destabilisation (Heezen et al., 1964; Khripounoff et al.,
291 2003). Mean values of water discharge Q_w in the Congo River were inferred from the literature
292 (41,000 m^3/s ; Laraque et al., 2009, 2013) and then extrapolated from multi-proxy studies, as
293 described in detail in section 3.4. The uncertainties ($\pm 4,000 \text{ m}^3/\text{s}$) were determined according to
294 the centennial fluctuations measured by Laraque et al. (2013).

295 Lithologies were limited to sand (grain size of 0.2 mm) and mud (grain size of 0.004 mm),
296 for which compaction laws (by default in the software) were used during simulations. We used a
297 diffusion coefficient for long-term gravity-driven transport of $10^{-2} \text{ km}^2/\text{kyr}$ for the marine domain
298 and $10^{-3} \text{ km}^2/\text{kyr}$ for the continental domain, which are reasonable values based on modelling
299 performed on similar sedimentary systems (e.g. Csato et al., 2013; Leroux et al., 2014; Deville et al.,
300 2015). For water-driven transport, we adopted the same values of the diffusion coefficient for long-
301 term and short-term water-driven transport. The calibration of these diffusion coefficients was
302 based on the longitudinal and lateral extents of the simulated deep-sea fan when the Q_w , Q_s , and
303 sand/mud ratio were kept constant. Figure 6 shows the high sensitivity of the final geometry of the
304 turbidite system in the deep-sea environment to the diffusion coefficient. Values of 1.5 and 10

305 km²/kyr, respectively, were chosen for $K_{water,sand}$ and $K_{water,mud}$ for all simulations because they
306 allowed the best reproduction of the general size (length and width) of the Axial Fan deposits.

307 **(iii) Sediment availability:** The mean value of sediment supply Q_s was first calculated from
308 the entire volume of the Axial Fan, 7,500 km³, which yielded a mean Q_s of 37 km³/kyr over 210 kyr.
309 The uncertainty related to the resolution of seismic data was ± 5 km³/kyr. Then, we defined
310 minimum and maximum values through time of Q_s based on a BQART approach (Syvitski et al.,
311 2003; Syvitski and Milliman, 2007) performed on the Congo River watershed, which allowed us to
312 fix extreme boundaries for Q_s in our models as a function of water discharge, basin area, maximum
313 relief, mean temperature, lithology, and trapping efficiency. Using this equation, the sediment flux
314 for the Congo River was quantified for both interglacial and glacial periods. Because of the narrow
315 and steep geometry of the margin, the basin area has remained unchanged over the last 210 kyr. We
316 assumed that the mean maximum relief and lithology also remained constant over the last 210 kyr.
317 We also kept the water discharge constant over time by taking the mean value reported by Laraque
318 et al. (2013). The mean temperature and trapping efficiency in the estuary are sensitive properties
319 related to glacial and interglacial fluctuations. Based on the Community Climate System Models
320 (CCSM – Kutzbach et al., 1998), the mean temperature between latitudes 30°N and 30°S was set at
321 15 °C during the Last Glacial Maximum and at 20 °C for interglacial periods. Regarding the
322 trapping efficiency, we tested two distinct configurations corresponding to the value assumed by
323 Moguelet (1988), who suggested that between one-third and two-thirds of conveyed sediment may
324 be trapped at the river mouth. Our results show that during the Last Glacial Maximum, the values of
325 sediment supply varied between 24 and 46 km³/kyr for a high and low trapping efficiency,
326 respectively. Similarly, for the last interglacial period, the sediment supply ranged between 32 and
327 62 km³/kyr.

328 The sand/mud ratio was inferred from core data (sedimentary logs of cores RZCS01,
329 RZCS06, RZCS07, RZCS15, RZCS21, and RZCS25 presented by Picot et al., 2019) and the

330 morpho-sedimentary map of Babonneau (2002) updated based on our interpretation of seismic
331 volumes of sand (channels) and mud (levees and distal fringes of lobes) facies. This approach
332 indicated relative proportions of sand and mud of 24% and 76%, respectively, during interglacial
333 periods and 30% and 70%, respectively, during glacial intervals for the entire turbidite system. We
334 estimated uncertainties of $\pm 4\%$, linked to the silty parts of cores, which are difficult to attribute to
335 one of these two grain-size classes. Figure 5 summarises all the main input parameters for all of our
336 simulations.

337

338 **3.4. Simulated scenarios**

339 Based on the assumptions made during the construction of the geological conceptual model
340 (see section 2.3), six main scenarios were tested in the stratigraphic modelling:

341 **Scenario 1 – Autogenic control:** As the current dynamics and sinuosity of individual
342 channels were not simulated in our model, only the internal factor of topographic compensation
343 could be addressed in our study. Topographic compensation is here related to the initial bathymetry
344 of the basin (before deposition) and the evolution of the geometry of the sediment deposits
345 themselves through time (e.g. Flood and Piper, 1997; Pirmez et al., 1997). This scenario consists of
346 maintaining all input parameters constant over time during simulations.

347

348 **Scenario 2 – Sediment fluxes calculated from the seismic volumes of deposits:** The
349 relevance of Q_s calculated from the seismic volumes of deposits for each sedimentary cycle of the
350 Axial Fan (i.e. volumes between depth-converted horizons mapped from a 2D seismic grid) was
351 tested. The seismic volumes were decompacted to determine the mass flux, using the porosity laws
352 of Allen and Allen (2005) for sand and mud. The obtained volumes appeared highly variable over
353 time—1,996 km³ for cycle A, 1,097 km³ for cycle B, 3,446 km³ for cycle C, and 962 km³ for the
354 youngest and still active cycle D. For a mean sediment density of 1.6 g/cm³, these values

355 correspond to Q_s of 25.9 km³/kyr between 210 and 130 ka, 16.4 km³/kyr between 130 and 75 ka,
356 50.3 km³/kyr between 75 and 11 ka, and 90.2 km³/kyr between 11 and 0 ka.

357

358 **Scenario 3 – Extrapolation of the hydrological regime of the Congo River:** The aim was
359 to determine whether turbidity current dynamics are the result of the long-term regime change in the
360 feeding river or short-term ‘catastrophic’ events related to single high-energy floods. For this
361 purpose, we used the module HEST (see section 3.1).

362

363 For the following scenarios 4, 5 and 6, we used marine proxies of water and sediment
364 discharge in reference core data to calculate the evolution of Q_s and Q_w through time in our
365 simulations. For this purpose, by indicating the maximum and minimum values of Q_s and Q_w
366 presented in section 3.3, we transcribed the curves of marine proxies in values of Q_s and Q_w over
367 time. Mean values of Q_s and Q_w calculated as described in section 3.3 were then verified based on
368 these calculated curves to verify the viability of the input data over time. In particular, this allowed
369 us to test the impacts of the continental climate and vegetation cover on sediment flux to the deep-
370 sea basin.

371 **Scenario 4 – West African monsoon:** Two distinct simulations were considered:

- 372 • (4a): Q_s and Q_w extrapolated from the West African monsoon curve of Caley et al. (2011)
373 (see Fig. 2b for the curve);
- 374 • (4b) and (4c): cycles with a period of 23 kyr for both Q_s and Q_w to test the impact of
375 precessional orbital cycles with similar sinusoidal evolution of Q_s and Q_w over time (4b)
376 and a 5 kyr phase shift between Q_w and Q_s (4c).

377

378 **Scenario 5 – Marine proxy of vegetation cover changes in the watershed in response to**
379 **arid and humid conditions:** Several studies have demonstrated the reliable use of the pollen

380 distribution of *Podocarpus* as a proxy for climate/vegetation impact on sediment transfers (Jahns,
381 1996; Dupont et al., 1998; Jahns et al., 1998; Marret et al., 1999; Dupont et al., 2000; Dupont et al.,
382 2007; Ledru et al., 2007). Dalibard et al. (2014) also suggested that the pollen ratio
383 *Podocarpus*/(*Podocarpus* + rainforest) provides a reliable representation of the nature and
384 latitudinal distribution of vegetation in West Africa. The *Podocarpus*/(*Podocarpus* + rainforest)
385 pollen curve built from the KZai-02 reference core (Dalibard et al., 2014; see Fig. 2a for location
386 and Fig. 2b for the curve) was used in the simulations. Two assumptions were tested—positive (5a)
387 and negative (5b) correlations between Q_s and Q_w through time.

388

389 **Scenario 6 – Marine proxy of the timing of fluvial discharge in the basin:** Gingele et al.
390 (1998) showed that the kaolinite/smectite ratio is a relevant proxy of the timing and intensity of
391 fluvial discharge of the Congo River (see Fig. 2b). We therefore used this ratio measured from the
392 KZai-02 marine core (Sionneau et al., 2010) to extrapolate both Q_s and Q_w over time, by
393 considering positive (6a) and negative (6b) correlations between these two parameters in the same
394 way as in scenario (5).

395

396 Finally, for the extrapolation of the evolution of grain size over time, we modulated the
397 sand/mud ratio calculated from seismic and core data using the zirconium/rubidium ratio (Zr/Rb)
398 (measured in the reference core KZai-02; Fig. 2b), with respect to the average sand and mud
399 proportions calculated for arid and humid periods (see section 3.3). Zr/Rb is known to be a good
400 proxy of grain size distribution and transport efficiency (e.g. Dypvik and Harris, 2001).

401

402

403

4. Results

404 Approximately 100 simulations were performed based on the six scenarios proposed above.
405 Herein, we focus only on the best-calibrated simulations that present similar overall volumes of
406 deposits in the deep-sea environment to that in the geological model of the Axial Fan (section 2)
407 and suitable general architecture and distribution of depocentres. The primary selection was based
408 on uncertainty analyses performed with CougarFlowTM (section 3.2) to test the viability of the total
409 volume of sediment deposits in the deep-sea environment compared with the Axial Fan. For the
410 selected scenarios, Monte-Carlo risk analysis showed good calibration of the total volume, with P50
411 varying between 7,284 and 7,353 km³ (50% of chance that the real response value is equal to or
412 greater than the P50 value), close to the volume of 7,500 km³ calculated from seismic and
413 bathymetric data for the Axial Fan. The results of these selected simulations were compared with
414 the Axial Fan through two distinct criteria: (i) the general distribution of turbiditic channels
415 illustrated by the simulated sand distribution compared with the traces of channels shown in the
416 bathymetry of the Axial Fan (Figs. 7, 8, and 9) and (ii) the distance to the avulsion point (DA) from
417 a reference point located at the canyon mouth (see section 2.2 for explanation) between the
418 simulations (in orange) and the Axial Fan (in blue, from Picot et al., 2016) (Fig. 10). DA is the best
419 architectural parameter to highlight the dynamics of prograding and retrograding cycles of the
420 turbidite system over time. When such cycles were identified, we calculated the simulated volume
421 of each cycle and compared it with the volume obtained from the seismic interpretation of the Axial
422 Fan (see section 3.4). It is important to note that none of the simulations succeeded in reproducing
423 the positions of the currently active channels of cycle D located on a high relief area in the northern
424 part of the fan (Figs. 7, 8, and 9). The positions of these channels therefore were not used as criteria
425 for the primary selection of the best simulations; their absence in our simulations is discussed below.

426 The results of channel distributions of the different simulated scenarios (see section 3.4) are
427 presented in Figure 7 for scenario 1 (autogenic control), scenario 2 (sediment fluxes calculated from
428 seismic volumes), and scenario 3 (extrapolation of the hydrological regime of the Congo River); in

429 Figure 8 for the simulations of the West African monsoon in scenario 4a (model of Caley et al.,
430 2011), scenario 4b (sinusoidal curves with a 23-kyr period), and scenario 4c (sinusoidal curves for
431 Q_w and sawtooth pattern for Q_w with a 23-kyr period); and in Figure 9 for simulations based on
432 proxies of the KZai-02 reference core with the different scenarios 5 (marine proxy of vegetation
433 cover changes in the watershed in response to arid and humid conditions) and 6 (marine proxy of
434 the timing of fluvial discharge in the basin). The preliminary comparison of channels and avulsion
435 distribution permitted us to exclude some scenarios. This was the case for scenarios 1, 2, and 3 (Fig.
436 7a, 7b, and 7c), as all avulsions occurred in a position that was too distal from the reference point,
437 300 to 400 km compared with the main avulsion points in the Axial Fan at 200 km (Fig. 2). In these
438 scenarios, we noted the absence of architectural cycles and the lack of middle-fan depocentres. In
439 scenarios 4b (Fig. 8b) and 6b (Fig. 9d), the simulated sediments were shifted too far to the south
440 compared with the real data, even going beyond the limit of the model.

441 Among the remaining simulations with general architecture very similar to the general
442 outline of the Axial Fan, the examination of simulated progradational/retrogradational cycles (with
443 the distance to avulsion points DA) constituted the last discriminant parameter to choose the best-fit
444 scenarios (Fig. 10). As noted earlier, DA highlights progradational/retrogradational cycles with
445 volumes of deposits that can be compared with volumes calculated based on seismic data for the
446 Axial Fan. Then, Monte-Carlo risk analysis was performed using CougarFlow™ for each simulated
447 architectural cycle to define the uncertainties of the results (see section 3.2). For scenarios 4a (Fig.
448 10a) and 6a (Fig. 10e), only three progradational/retrogradational cycles were simulated, whereas
449 four cycles were observed in the Axial Fan. Scenario 5a was also rejected, even though the timing
450 of the main avulsion points was consistent with that of the Axial Fan. However, the distances to the
451 avulsion point defining the last cycle D and the end of cycle C did not fit with the geological reality
452 (Fig. 10c).

453 Consequently, two scenarios were able to reproduce the Axial Fan architectural evolution,
454 regarding the timing and position of up-fan avulsions and the simulated volumes of
455 progradational/retrogradational sedimentary cycles: (i) scenario 4c, corresponding to precession
456 cycles with a sawtooth pattern of Q_s and sinusoidal evolution of Q_w (Fig. 10b), and (ii) scenario 5b,
457 simulating arid/humid conditions inferred from the *Podocarpus*/(*Podocarpus* + rainforest) pollen
458 ratio with a negative correlation between Q_s and Q_w over time (Fig. 10d). For the sake of simplicity,
459 we refer to these best-fit models hereafter as the precession simulation for scenario 4c and the
460 vegetation simulation for scenario 5b.

461 It should be pointed out that even with these best-fit simulations, some differences exist with
462 respect to the architectural parameters calculated by Picot et al. (2016) for the Axial Fan. The first is
463 an additional volume of around 500 km³ for the first cycle A, between 210 and 130 ka. This
464 difference may be explained by the fact that the total longitudinal extent of this cycle is unknown
465 (bathymetric and seismic data are lacking in the most distal part of the basin). Another difference
466 arises for cycle C, for which simulations show a well-developed symmetrical
467 progradational/retrogradational cycle not observed by Picot et al. (2019). This difference may be
468 related to the lack of architectural data for the early part of cycle C because of the existence of a
469 cluster of stacked channels and lobes ('undifferentiated unit package 2' of Picot et al., 2019) for
470 which it was not possible to measure avulsion lengths. Lastly, for both simulations, we observed a
471 time shift of cycles B and A covering the period between 70 and 200 ka, for which the time
472 constraints are poor and possibly not accurate (Picot et al., 2019). Indeed, to achieve a perfect match
473 of the timing of these cycles, it appears to be necessary to shift the simulation curves approximately
474 10 kyr older during this period.

475

476

477 **5. Interpretation and discussion**

478 **5.1. Best-fit simulations versus geological model over the last 38 kyr**

479 Several studies have claimed that the timing and positions of channel avulsions, which
480 govern the architectural evolution of deep-marine fans, are linked to the interconnection over time
481 between both internal (such as topographic compensation, current dynamics, and channel sinuosity)
482 and external controls (such as tectonics and climate) (Kolla, 2007; Stouthamer and Berendsen,
483 2007). Deciphering the respective importance of distinct forcings is challenging, and our 3D
484 stratigraphic modelling is a useful tool in the attempt to individualise the relative effects of these
485 controls. Our results showed the following.

486 (1) Topographic compensation (the only internal control tested by our model) played a
487 minor role in the development of progradational/retrogradational cycles at the resolution scale of
488 the simulation, as shown by the poor calibration of the simulation testing autogenic control
489 (scenario 1; Fig. 7a), and more specifically in the development of up-fan avulsions (Fig. 11). Levee
490 instabilities and breaching (e.g. Ortiz-Karpf et al., 2015), which are not simulated in
491 DionisosFlowTM, are rarely observed in the Late Quaternary Congo Fan (Babonneau, 2002; Picot et
492 al., 2016), which suggests that such processes can be neglected here. This finding highlights the
493 dominant role of external controls on prograding/retrograding cycles.

494 (2) Catastrophic events do not simulate the most proximal up-fan avulsions. Scenario 2
495 aimed to test the calculation of sediment discharge based on the volume of sedimentary deposits
496 within each prograding/retrograding cycle defined by Picot et al. (2016, 2019). Such a simulation
497 necessarily implies a step-like evolution of sediment discharge and consequently rapid variations
498 through time. This explains why only one channel was active throughout the simulation (Fig. 7b),
499 as it was re-used with each sudden increase of sediment supply. The same explanation can be
500 proposed for the simulation that used the module of catastrophic high-energy events (scenario 3; Fig.
501 7c). It appears that a more progressive evolution of sediment and water discharge is necessary to
502 produce separated channel systems and thus individual progradational/retrogradational cycles.

503 (3) Consequently, we can first confirm through stratigraphic modelling that the impact of
504 climate changes on Q_s and Q_w is a dominant influence on the architectural evolution of the deep-
505 sea fan, as shown by the two best-fit simulations based on the precession cycle controlling the West
506 African monsoon (Caley et al., 2011) and the change of vegetation cover based on the pollen proxy
507 in marine cores.

508 Fan activity during the last 38 kyr corresponds to the best-constrained chronostratigraphic
509 interval based on the work of Picot et al. (2019), and allows the viability of our simulations to be
510 assessed (Fig. 12). Both of the best simulations, the precession and vegetation scenarios (scenarios
511 4c and 5b respectively), show very well-suited evolution of progradation and retrogradation during
512 this period, with nearly perfect superposition of the curves showing the distance of avulsion points
513 over time (Fig. 10b and 10d). The slight time shift of curves was likely only caused by the large
514 time step of 5 kyr. Between 38 ka and 28 ka, a general progradation of the system was indicated
515 (Fig. 13a-t1), with sediments transported to the down-fan area more than 700 km away from the
516 canyon mouth. Cross-sections in the simulations reveal prograding clinoforms that exhibit
517 similarities with geometries observed in longitudinal seismic profiles of the Axial Fan (Fig. 13b).
518 The down-fan area is mainly characterised by muddy deposits with approximately 85% mud, which
519 is quite consistent with the piston core observations indicating 82% \pm 4% mud in the terminal
520 lobes. This period of progradation corresponds to the end of MIS 3, which was a humid climate
521 stage (Schneider et al., 1997; Dupont et al., 2000) (Fig. 12), consistent with the geological model of
522 Picot et al. (2019). In our simulations, the Q_w of the Congo River increased and the Q_s was low.
523 These conditions correspond to an important transport capacity explaining the maximal
524 progradation of the sediments (Mutti and Normark, 1987; Reading and Richards, 1994; Galloway,
525 1998). At the climatic transition between humid (MIS 3) and arid (MIS 2) periods, an aggradation
526 of depocentres occurred just before large-scale retrogradation (Fig. 12 and 13a-t2), possibly related
527 to a backfilling effect of channelised structures (Fig. 11), as also indicated by Hodgson et al. (2006)

528 based on their ‘tripartite model’ in the Karoo Basin. Such a process would progressively lead to the
529 retrogradation of depocentres, characterised by several middle-fan avulsions. Middle-fan avulsions
530 would create well-individualised laterally migrating depocentres, which are comparable with those
531 observed in the seismic data (Fig. 13c). The retrogradation of the system started when Q_s and the
532 sand fraction were at their maxima; that is, when the Congo River exhibited its minimum transport
533 capacity. The retrogradation progressively continued as Q_w and Q_s decreased until the arid/humid
534 climatic transition at 15 ka. This transition was marked by a proximal up-fan avulsion located less
535 than 200 km from the submarine canyon mouth, showing overall northward stacking of sand-rich
536 deposits over time (Fig. 13d). Up-fan avulsion was directly followed by an abrupt progradation of
537 depocentres marking the onset of the currently active cycle D (Fig. 13a-t3 and 13d). Up-fan
538 avulsion and progradation during the humid period was a consequence of the significant increase in
539 river transport capacity while the sediment charge conveyed was still low and Q_w was increasing
540 (Fig. 13a-t3).

541 However, a significant difference from the geological model of the Axial Fan was associated
542 with the position of the currently active turbidite channel in the northern part of the system,
543 abnormally perched on the previous Northern Fan (Fig. 2a and 14). None of our simulations
544 successfully simulated the correct position of this channel. The best-fit simulations showed an
545 active channel in the northern part, but it was limited northward by the elevation of the Northern
546 Fan (Fig. 14). The position on a topographic high and the overdeepening of the current active
547 channel of the Axial Fan are attributed to very muddy flow over a long period of time, which
548 concentrated turbulence at the base of the channel through the construction of high external levees
549 (Babonneau et al., 2010). In this configuration, greater development of external levees by flow
550 stripping and overspill of the muddy material is associated with greater turbulence, and therefore
551 increased channel deepening. Our model does not simulate these local turbulences, which explains
552 why the simulated turbidity currents did not migrate on the high points of the Northern Fan.

553 Despite the position of the currently active turbidite channel, the simulated progradation and
554 retrogradation phases during the last 38 kyr are consistent with the geological model of Picot et al.
555 (2019). The stratigraphic modelling thus confirms that the variation of liquid and solid discharge in
556 response to climate/vegetation coupling in the watershed was the main forcing factor of the
557 progradational/retrogradational cycles.

558

559 **5.2. Extrapolation to 210 kyr**

560 The precession and vegetation simulations have thus been validated by the well-calibrated
561 chronostratigraphic model of Picot et al. (2019) between 0 and 38 ka. We now aim to extrapolate
562 these models on a longer time scale over the last 210 kyr.

563 For both the precession and vegetation simulations, the results show the succession of four
564 main progradational/retrogradational cycles, respectively between 210 and 130 ka, 130 and 85 ka,
565 85 and 15 ka, and 15 and 0 ka (Fig. 10B, 10d and 14). Each cycle is characterised by the same
566 geometric evolution, which can be sequentially divided into the three steps as described in section
567 5.1: (i) up-fan avulsion followed by (ii) maximum progradation of depocentres, and (iii) progressive
568 retrogradation of the system (Fig. 13a). The curves of the distance to avulsion points from
569 geological data and from simulations can be superimposed with a time shift of approximately 10
570 kyr (Fig. 10b and 10d), which confirms that the architectural evolution of the fan over the last 210
571 kyr was accurately reproduced. The time shift may be explained by the time step of the simulations,
572 and also by the uncertainties of ages obtained from dating based in geological data, as these dates
573 are not yet sufficiently accurate at this time scale. The conceptual architectural model defined in
574 section 2 for the last 38 kyr thus seems to be applicable to the entire activity period of the Axial Fan.

575 Over the last 210 kyr, sedimentation has been controlled by the concomitant variation of
576 sediment and water discharge in response to climate changes. Retrogradation of the turbidite system
577 has always been initiated when the sediment discharge was high and the river runoff decreased

578 during arid periods (Fig. 12). Following these retrogradational periods, proximal up-fan avulsions
579 and maximum depocentre progradation were induced by maximum water discharges and minimum
580 conveyed sediment loads at the arid/humid climate transition. However, the mechanism of middle-
581 fan avulsions is different from that involved in large-scale up-fan avulsions. Our simulations show
582 that up-fan avulsions are linked to high-magnitude variations of the volume of sediment transported
583 from the continent to the sedimentary basin. In contrast, the development of middle-fan and down-
584 fan avulsions was more sensitive to the evolution of the sand fraction in the sediment supply, as
585 these events were always synchronous with abrupt increase of the sand fraction and thus directly
586 linked to the decrease in flow transport efficiency (Mutti and Normark, 1987; Reading and Richards,
587 1994; Galloway, 1998). We assume that this abrupt increase of sandy material (Fig. 12) may be
588 linked to the destabilisation and transfer of river mouth sand bars observed in the present at the head
589 of the canyon during high river runoff and canyon flushing events (Moguedet, 1988).

590

591 **5.3. Source-to-sink interpretation: climate/vegetation coupling**

592 We have confirmed that climate/vegetation coupling controlled the architecture of the fan
593 throughout its entire period of sedimentation. Interpretation of the input data of our simulations
594 allowed identification of the geological forcing parameters involved in the architectural evolution of
595 the fan.

596

597 ***Implications of the precession simulation***

598 Among all the simulations controlled by precession, we herein highlight the need to
599 simulate a sawtooth pattern of Q_s with an abrupt rise, often synchronous with an increase in the
600 sand fraction, followed by a gradual drop (Fig. 12). Abrupt increase in Q_s induces major
601 retrogradation of the turbidite system as the transport capacity decreases. The maximum Q_s , coeval
602 with a high Q_w and high sand fraction, likely indicates the direct transfer of sediment from the

603 continent to the deep-sea basin during river flooding that caused the destabilisation of sandy river
604 mouth bars (Moguedet, 1988). Unlike some models for turbidite systems, such as the Makran
605 system (Bourget et al., 2011), even though arid climate conditions in the Congo River watershed
606 induced enhanced mechanical erosion in comparison with chemical weathering, such conditions do
607 not imply the development of large sandy turbidites. Rather, an arid climate in the Congo watershed
608 is more favourable to temporary trapping of coarse-grained sediments during aggradation of river
609 channel beds (e.g. Blum and Straffin, 2001), floodplain storage (Molliex et al., 2019), and the
610 formation of river mouth bars at the entry of the submarine canyon (Moguedet, 1988). The trapping
611 of coarse-grained materials persisted until river runoff was sufficient to convey such a load, marked
612 by a maximum Q_w in the simulation. In contrast with the hypothesis of Picot et al. (2019), which
613 related proximal up-fan avulsions to an increase in sediment load, the simulated proximal up-fan
614 avulsions corresponded to an increase in the river runoff Q_w and a drop of the conveyed sediment
615 load Q_s (Fig. 12). In the precession simulation, the up-fan avulsion and the following major
616 progradation of the system were only caused by the increase of turbidity current transport capacity
617 when the monsoon intensity was high and chemical weathering was predominant on land, implying
618 a large mud supply in the turbidite environment.

619

620 ***Implications of the vegetation simulation***

621 The vegetation simulation showed similar architectural evolution to that of the precession
622 simulation, despite differences in inputs. The evolution of Q_w in both simulations was very similar,
623 whereas the evolution of Q_s differed. The Q_w is probably more important than Q_s in the timing of
624 progradational/retrogradational cycles because when the sediment load is high, considerable water
625 discharge is needed to efficiently transport sediments from the continent to the deep-sea
626 environment. Consequently, the difference in Q_s evolution between the two simulations represents a
627 difference in the geological process of sediment production and trapping on land. In the vegetation

628 simulation, the maximum sediment production occurred during arid periods, and sediments were
629 trapped until the maximum water discharge was reached. The curve of continental vegetation
630 changes in our simulation was used as a proxy of the modifications of vegetation cover in the
631 Congo watershed in response to successive humid/arid climate oscillations, themselves governed by
632 the West African monsoon (Hoelvoeth et al., 2001; Weldeab et al., 2007; Dupont, 2011; Dalibard et
633 al., 2014). That is why the use of this curve yielded the same results as the precession simulation
634 that simulates the variations of monsoon intensity. Expansion of vegetation cover is expected to
635 decrease the magnitude of river runoff and the sediment yield, according to the balance between
636 mechanical and chemical erosion, because of the reduction of rainfall impact, modification of soil
637 moisture, increased infiltration, increased evapotranspiration, root mechanical reinforcement, and
638 increased surface stability favoured by the weight of vegetation (e.g. Renard et al., 1997). This
639 concept implies a negative correlation over time between vegetation cover and soil erosion and
640 runoff (e.g. Gaillardet et al., 1999; Zhou et al., 2008; Hou et al., 2016), and thus a negative
641 correlation between water and sediment discharge over time, as demonstrated in the Nile River
642 (Krom et al., 2002; Ducassou et al., 2009), the Niger Delta (Zabel et al., 2001), and the Bengal Fan
643 (Weber et al., 2003). Our vegetation simulation results are consistent with these observations, with
644 the best simulation obtained through a negative correlation between Q_s and Q_w over time (Fig. 12).

645

646 **5.4. Insights and limits of diffusion process-based stratigraphic modelling**

647 Since the 1990s, 3D forward modelling has been used to test hypotheses in geological
648 conceptual models through an ‘inversion loop’ that helps to extrapolate field and geophysical data
649 when the resolution is temporally or spatially limited. However, very few process-based modelling
650 studies have attempted to reproduce the architectural evolution of turbidite systems along the deep-
651 marine domain at the basin-scale (e.g. Groenenberg et al., 2009; Groenenberg et al., 2010;
652 Gvirtzman et al., 2014; Deville et al., 2015; Hawie et al., 2018).

653 This study shows that a nonlinear water-driven diffusion equation allows the reproduction of
654 basinward/landward migration of depocentres over time with channelised systems whose geometry
655 is comparable to channel–levee–lobe systems observed in geophysical data (Figs. 13 and 14). The
656 resolution scale of stratigraphic modelling is similar to the horizontal resolution of geophysical data,
657 which permits comparison with architectural parameters measured in the simulations and those
658 measured directly through geophysical interpretation. In addition, the numerical approach allows
659 interpolation between seismic lines (in our case, spacing of 2D seismic acquisition can reach 26 km,
660 four times the resolution of the stratigraphic grid in our model) and provides simulated total
661 volumes of sediments deposited in the area, including the extrapolation of zones not fully covered
662 by geophysical and core data (both laterally and vertically). Furthermore, the simulation provides
663 better 3D distribution of the lithological facies (sand/mud ratio), especially at depths that cannot be
664 reached by piston cores (which usually reach maximum depths of 20–30 m), and thus reveals
665 crucial information to understand reservoir quality. Most importantly, this numerical modelling
666 provides quantification of the sediment flux over time and permits independent investigation of the
667 relative impacts of Q_s , Q_w , and the sand fraction in the Congo turbidite depocentres defined based
668 on various internal and external factors. Our simulations demonstrate the relevance of using climate
669 and environmental proxy curves (such as pollen, $\delta^{18}\text{O}$, and kaolinite/smectite) to simulate the
670 sediment supply from source to sink in this type of stratigraphic modelling.

671 However, some caution must be taken when the processes at the origin of the depositional
672 stacking pattern are interpreted, as diffusion process-based modelling averages the mechanisms of
673 sediment transport and deposition at a given time step. Therefore, we must assume that all
674 geological processes acting in the turbidite system dynamics can be averaged within a 5 kyr period
675 in our study. This assumption is not true at the scale of individual channels with activity that
676 extends from 1 to several kyr, according to Picot et al. (2019). Other external forcings are also
677 ignored because of this time scale, such as semi-precession cycles with periods of 5.5 to 11.5 kyr

678 (Berger and Loutre, 1997) or Heinrich cycles with periods of 6 to 8 kyr (Weldeab et al., 2007),
679 which have been suspected by Dalibard et al. (2014) and Picot et al. (2016) to play a role in the
680 development of sedimentary sub-cycles in the Late Quaternary Congo Fan. However, because our
681 objective was to analyse the controlling parameters responsible for the development of long
682 progradational/retrogradational sedimentary cycles, the use of diffusion process-based modelling is
683 relevant here.

684 Our forward stratigraphic model extrapolates the geological processes on land from marine
685 data, which necessarily implies uncertainties in the interpretations. First, the response time between
686 the climate, geological processes, and sediment yield on land is not well known, especially for large
687 watersheds such as the Congo sedimentary system (Gasse, 2000). Second, it is challenging to
688 evaluate the timing of sediment transfers toward deep-marine basins. Ducassou et al. (2009)
689 reported an instantaneous response of the river and submarine fan to millennial-scale changes in
690 climate in the Nile drainage system, with a time scale compatible with the time resolution of our
691 model. In the case of the Congo Fan, the turbidite system is permanently connected to the feeding
692 river through the submarine canyon; therefore, we assume that the behaviour of the submarine
693 sedimentary system also reflects the geological processes in the watershed. Molliex et al. (2019)
694 modelled the hydro-sedimentary evolution for the Congo River watershed over the last 155 kyr
695 using the HydroTrend model (Syvitski et al., 1998; Kettner and Syvitski, 2008). Incorporating the
696 evolution of the HydroTrend model sediment discharge in DionisosFlowTM failed to reproduce the
697 geological model. Instead, the simulation showed the activity of only one channel that avulsed
698 exclusively in the most distal part of the deep-marine basin. The main reason for this inconsistency
699 was that only the suspended sediment load was simulated by Molliex et al. (2019), even though
700 coarse-grained material represents up to 30% of the sediment budget in the Late Quaternary Congo
701 Fan and is probably transported as bedload. An abrupt supply of sandy sediments induces a
702 decrease in turbidity current transport capacity and thus can be responsible for avulsion and

703 retrogradation of the fan and is of primary importance in the architectural evolution of the fan.
704 Catastrophic destabilisations of sandy river mouth bars at the head of the submarine canyon may
705 play a key role in the architectural evolution of the deep-sea fan, but the sedimentary processes in
706 the estuarine zone of the Congo River are not well known. In addition, a large portion of the eroded
707 matter of the Congo watershed is transported as dissolved load. This silica-rich dissolved load may
708 quickly precipitate via biogenic processes when it reaches the marine environment, thus strongly
709 increasing the sediment supply through the formation of siliceous biogenic sediment (comprising
710 between 5% and 30% of Congo-fan deposits; Schneider et al., 1997; Hatin et al., 2017), or via rapid
711 degradation into authigenic K- and Fe-rich aluminosilicates (Michalopoulos and Aller, 2004),
712 which are also present in the Congo Fan deposits (Giresse et al., 1998). In addition, coastal currents
713 and tidal effects have not yet been implemented in DionisosFlowTM, although the impacts of such
714 currents on sediment transport are assumed to be weak compared with the hyperpycnal flows in the
715 case of the Congo River. Consequently, our work demonstrates that the extrapolation of marine
716 proxies of climatic and environmental changes in the watershed is an efficient tool to recreate the
717 3D architecture of turbidite systems, although progress must be made in linking stratigraphic
718 modelling with onshore hydrogeological simulations to construct a complete source-to-sink
719 geological model.

720

721 **6. Conclusions**

722 This study presents for the first time the use of the diffusion process-based stratigraphic
723 forward model DionisosFlowTM to constrain the progradation/retrogradation cycles of a submarine
724 fan at the basin-scale, by examining the case of the Late Quaternary Congo Fan. Simulation
725 viability was tested based on the geological model proposed by Picot et al. (2019), which
726 emphasises the role of climate changes and the impact of induced geological processes on the
727 architectural evolution of the fan during the last 38 kyr. Our main objective was first to confirm this

728 model through numerical modelling and then to attempt to extrapolate it throughout the entire
729 activity period of the fan over the last 210 kyr, a period not well constrained by dating methods.
730 This diffusion process-based model was found to be a reliable and efficient tool for the simulation
731 of sedimentary progradation/retrogradation cycles as a function of marine and continental proxies.

732 Several key points must be retained from this work:

733 • Simulations modelled the correct organisation of the channel-lobe system in the deep-sea
734 environment using a nonlinear diffusion equation for sediment transport.

735 • The horizontal and vertical resolutions of this model were high enough to verify the
736 viability of simulations through comparison with geophysical and marine core data. Once validated,
737 the simulations also allowed us to image sediment deposits where geophysical data were lacking,
738 such as between seismic lines and marine cores.

739 • The water-driven diffusion process-based model permitted us to study the relative impacts
740 of the variations of sea-level, tectonics, sediment and water discharges, and the sand fraction on the
741 behaviour of the turbidite system. Forward stratigraphic modelling provided the opportunity to test
742 an infinite number of scenarios, particularly with input data defined from marine and continental
743 proxies of climate changes. Consequently, the architectural evolution of the submarine fan could be
744 linked to geological changes in the watershed through a source-to-sink approach. Our best-fit
745 scenarios confirmed that climate/vegetation coupling was the main forcing factor in the
746 architectural evolution of the Late Quaternary Congo Fan over the last 210 kyr.

747 • The interpretation of hydrogeological processes on the continent established here for the
748 Late Quaternary Congo sedimentary system cannot be generalised for all turbidite systems, as the
749 perennial connection between the Congo River and the submarine canyon induced a direct response
750 between sedimentary processes on land and sediment transfer to the deep-sea fan.

751 • Source-to-sink analysis by incorporating output data of HydroTrend hydrological modelling
752 of the Congo River watershed (Molliex et al., 2019) was not found to be viable, primarily because

753 only the suspended load fraction was modelled at the outlet of the watershed, not the bedload.
754 Therefore, efforts are still required to improve the integration of continental hydro-sedimentary
755 modelling with stratigraphic modelling in the deep-sea environment.

756 Knowledge of the stratigraphic evolution of deep-marine sedimentary systems helps us to
757 understand the architecture of economic reservoirs (for energy, storage, etc.) as well as potential
758 terrestrial pollutants, as turbidite systems are considered major sinks for wastes conveyed by rivers,
759 particularly microplastics (Kane et al., 2019).

760 **Figure captions**

761

762 **Figure 1:** a. Map of the Congo sedimentary system from the Congo River watershed to the Late
763 Quaternary submarine fan (modified from Picot et al., 2019). b. Three-dimensional view of the
764 Congo sedimentary system reconstructed from the compilation of bathymetric data from the
765 Guinness (Cochonat and Robin, 1992; Cochonat, 1993), Zaiango (Cochonat, 1998; Savoye, 1998),
766 and Reprezaï (Marsset and Droz, 2010; Droz and Marsset, 2011) oceanographic cruises and
767 ETOPO1 (Amante and Eakins, 2008) in the watershed (vertical exaggeration x30). Red boxes
768 indicate the sediment budget from the Congo River to the submarine fan. Black boxes illustrate the
769 forcing factors potentially controlling the sediment supply in the watershed and deposition in the
770 deep-sea environment. The location of the reference marine core KZai-02 is indicated.

771

772 **Figure 2:** Geological interpretation of the Axial Congo Fan (210 kyr to present) from Picot et al.
773 (2016, 2019). a. Channel-lobe map with the location of the reference core KZai-02 (red star). b.
774 Multi-proxy study. From left to right: architectural diagrams of the fan (channel length in dark blue,
775 distance of avulsion points in light blue—see the sketch below for explanation), $\delta^{18}\text{O}$ curve of
776 Lisiecki and Raymo (2005), proxies from the reference core KZai-02, *i.e.*, the
777 *Podocarpus*/(*Podocarpus* + rainforest) pollen ratio (Dalibard et al., 2014), kaolinite/smectite ratio
778 (Sionneau et al., 2010), zirconium/rubidium (Zr/Rb) ratio (Picot et al., 2019), and West African
779 monsoon curve (Caley et al., 2011). The grey areas correspond to the timing of increased sediment
780 flux in the marine environment inferred from the variations of the kaolinite/smectite ratio (Sionneau
781 et al., 2010).

782

783 **Figure 3:** Geological conceptual model proposed by Picot et al. (2019) emphasising the role of
784 humid/arid climate fluctuations in the architectural evolution of the Congo Axial Fan during the last
785 38 kyr. See the text for explanation.

786

787 **Figure 4:** Inversion loop illustrating the simulation strategy of 3D forward stratigraphic modelling
788 performed with DionisosFlowTM supplemented by uncertainty analysis conducted with
789 CougarFlowTM. The confrontation between the geological conceptual model and modelling results
790 is crucial to obtain a relevant source-to-sink model of the architectural evolution of the study area
791 and to test the roles of the different forcing factors of sedimentation.

792

793 **Figure 5:** Model setup for the 3D forward stratigraphic modelling. Top: initial bathymetry at 210 ka
794 in the simulation (base surface of the Axial Fan) and position of the sediment source. Below:
795 synthesis of the different input parameters described in the text.

796

797 **Figure 6:** Simulated sand thickness in the fan as a function of the water-driven diffusion
798 coefficients for sand ($K_{water,sand}$) and mud ($K_{water,mud}$). The intermediate configuration was chosen for
799 our simulations ($K_{water,sand} = 1.5 \text{ km}^2/\text{kyr}$; $K_{water,mud} = 10 \text{ km}^2/\text{kyr}$).

800

801 **Figure 7:** Distribution of simulated sand thickness in the deep-sea environment at the end of
802 simulation for scenarios 1 (autogenic control), 2 (Q_s calculated from the volume of deposited
803 sediment deduced from seismic data), and 3 (extrapolation of the hydrological regime of the Congo
804 River). Axial Fan channels from Picot et al. (2016) are reported on the maps (orange line: currently
805 active channel; black lines: preceding channels). The point R is the reference point used by Picot et
806 al. (2016) and in this study to measure the distance to avulsion points.

807

808 **Figure 8:** Maps illustrating the distribution of sand thickness in the deep-sea environment at the end
809 of simulation of scenario 4, the West African monsoon: (4a) monsoon model of Caley et al. (2011);
810 (4b) precession: 23 kyr cycle with concordant sinusoidal curves for Q_s and Q_w ; (4c) precession: 23
811 kyr cycle with sinusoidal curves for Q_w and a sawtooth pattern of Q_s with a time shift of 5 kyr
812 between the two curves. Axial Fan channels from Picot et al. (2016) are reported on the maps
813 (orange line: currently active channel; black lines: previous channels). The point R corresponds to
814 the reference point explained in Fig. 7.

815

816 **Figure 9:** Maps illustrating the distribution of sand thickness in the deep-sea environment at the end
817 of simulations for the scenarios of: the impact of vegetation cover based on the pollen ratio of
818 *Podocarpus*/(*Podocarpus*/rainforest) in the KZai-02 marine core with scenario 5a (positive
819 correlation of Q_s and Q_w over time) and scenario 5b (negative correlation of Q_s and Q_w over time);
820 the timing of fluvial discharge based on the kaolinite/smectite ratio in the KZai-02 marine core with
821 positive (scenario 6a) and negative (scenario 6b) correlations of Q_s and Q_w over time. Axial Fan
822 channels from Picot et al. (2016) are reported on the maps (orange line: currently active channel;
823 black lines: previous channels). The point R corresponds to the reference point explained in Fig. 7.

824

825 **Figure 10:** Left: Architectural diagrams of best-fit simulations illustrating the evolution of distances
826 (km) to avulsion points (light blue) compared with the same parameter calculated from the
827 geological model of the Axial Fan (green) (Picot et al., 2019). Right: Volume (km^3) of
828 progradational/retrogradational cycles (dark blue: simulated volumes in DionisosFlowTM; brown:
829 volumes in the Axial Fan calculated from seismic interpretation).

830

831 **Figure 11:** Three-dimensional view of the turbidity flow pathway (in red) during the main avulsion:
832 a. t1 – Initial configuration before avulsion. b. t2'– Middle-fan avulsion simulated in scenario 1,

833 autogenic control, which essentially considered the role of topographic compensation. c. Up-fan
834 avulsion simulated in the vegetation simulation.

835

836 **Figure 12:** Evolution over time of the input parameters Q_s and Q_w for the vegetation simulation
837 (red bold lines) and the precession simulation (purple dashed lines), and the sand fraction in green,
838 which was similar in both simulations. The timing of simulated up-fan (bold black lines) and
839 middle-fan (dashed black lines) avulsions is also indicated, as well as progradational and
840 retrogradational phases in the right part of the graph (black arrows). MIS: Marine Isotope Stage;
841 grey and white horizontal bands: arid and humid periods, respectively.

842

843 **Figure 13:** Architectural evolution of a sedimentary cycle obtained in both best-fit simulations
844 (vegetation and precession simulations). a. Successive stages of an architectural cycle illustrated
845 from the distribution of channel deposits (in red), lobe deposits (sandy in yellow and muddy in
846 orange), and overflow muddy deposits (in black): (t1) maximum progradation, (t2) aggradation and
847 retrogradation, and (t3) up-fan avulsion. E–W-oriented white arrows: progradation or retrogradation
848 directions; N–S-oriented white arrows: lateral migration of depocentres. The circles indicate the
849 relative proportions of sand and mud calculated in the simulation. b. and c. Comparison between
850 cross-sections of the sand fraction in the simulations and seismic profiles in the Late Quaternary
851 Congo Fan for (b) the progradational phase (AA', location at a-t1) and (c) the retrogradational phase
852 associated with middle-fan avulsions (BB', location at a-t2). d. Block diagrams showing the water
853 discharge value (m^3/s) (illustrating the turbidity flow pathway) in the simulation during the up-fan
854 avulsion events. CC' is a cross-section of the sand fraction in the proximal avulsion node (location
855 at a-t3).

856

857 **Figure 14:** Transverse cross-section of the middle-fan zone across the final geometry of the
858 vegetation simulation (see Fig. 9b for location). This section illustrates the overall northward
859 migration of architectural cycles (A, B, C, and D) over time, as well as the incorrect positions of the
860 simulated active cycles, which are not positioned on the topographic high formed by the Northern
861 Fan as is the case in the real fan.

862

863 **Bibliography**

- 864 Allen, P., Allen, J., 2005, Basin analysis, Principles and Applications, 549 pp., Blackwell Publishing Ltd,
865 Second Edition.
- 866 Alsdorf, D., Beighley, E., Laraque, A., Lee, H., Tshimanga, R., O'Loughlin, F., Mahé, G., Dinga, B.,
867 Moukandi, G., Spencer, R.G.M., 2016. Opportunities for hydrologic research in the Congo Basin. *Rev.*
868 *Geophys.* 54, 378–409.
- 869 Alzaga-Ruiz, H., Granjeon, D., Lopez, M., Seranne, M., Roure, F., 2009. Gravitational collapse and Neogene
870 sediment transfer across the western margin of the Gulf of Mexico: Insights from numerical models.
871 *Tectonophysics* 470, 21–41.
- 872 Amante, C., Eakins, B. W., 2008. ETOPO1 1 Arc-Minute Global Relief Model: Procedures, Data Sources
873 and Analysis, National Geophysical Data Center, NESDIS, NOAA, US Dept. Commerce, Boulder, CO,
874 USA.
- 875 Anka, Z., Séranne, M., Lopez, M., Scheck-Wenderoth, M., Savoye, B., 2009. The long-term evolution of the
876 Congo deepsea fan: A basin-wide view of the interaction between a giant submarine fan and a mature
877 passive margin (ZaiAngoproject). *Tectonophysics* 470, 42–56.
- 878 Anka, Z., Séranne, M., 2004. Reconnaissance study of the ancient Zaire (Congo) deep-sea fan.(ZaiAngo
879 Project). *Mar. Geol.* 209, 223–244.
- 880 Armitage, D.A., McHargue, T., Fildani, A., Graham, S.A., 2012. Postavulsion channel evolution: Niger
881 Delta continental slope. *Am. Assoc. Pet. Geol. Bull.* 96, 823–843.
- 882 Babonneau, N., Savoye, B., Cremer, M., Bez, M. (2010). Sedimentary architecture in meanders of a
883 submarine channel: detailed study of the present Congo turbidite channel (Zaiango project). *Journal of*
884 *Sedimentary Research*, 80(10), 852-866.
- 885 Babonneau, N., 2002. Mode de fonctionnement d'un chenal turbiditique méandriforme: Cas du Système
886 Turbiditique actuel du Zaïre. PhD thesis, Univ. Bordeaux I, Bordeaux. Université Bordeaux 1.
- 887 Berger, A., Loutre, M.F., 1997. Intertropical latitudes and precessional and half-precessional cycles. *Science*
888 (80-). 278, 1476–1478.
- 889 Blum, M.D., Straffin, E.C., 2001. Fluvial responses to external forcing: examples from the French Massif
890 Central, the Texas Coastal Plain (USA), the Sahara of Tunisia, and the lower Mississippi Valley (USA).
891 *River Basin Sediment Syst. Arch. Environ. Chang. Balkema, Rotterdam* 195–228.
- 892 Bourget, J., Zaragosi, S., Ellouz-Zimmermann, N., Mouchot, N., Garlan, T., Schneider, J., Lanfumey, V.,
893 Lallemand, S., 2011. Turbidite system architecture and sedimentary processes along topographically
894 complex slopes: the Makran convergent margin. *Sedimentology* 58, 376–406.
- 895 Broucke, O., Temple, F., Rouby, D., Robin, C., Calassou, S., Nalpas, T., Guillocheau, F., 2004. The role of
896 deformation processes on the geometry of mud-dominated turbiditic systems, Oligocene and Lower
897 Middle Miocene of the Lower Congo basin (West African Margin). *Mar. Pet. Geol.* 21, 327–348.
- 898 Brovkin, V., Claussen, M., Petoukhov, V., & Ganopolski, A. (1998). On the stability of the atmosphere-
899 vegetation system in the Sahara/Sahel region. *Journal of Geophysical Research: Atmospheres*,
900 103(D24), 31613-31624.

- 901 Burgess, P. M., Masiero, I., Toby, S. C., Duller, R. A., 2019. A big fan of signals? Exploring autogenic and
902 allogenic process and product in a numerical stratigraphic forward model of submarine-fan
903 development. *Journal of Sedimentary Research*, 89(1), 1-12.
- 904 Caley, T., Malaizé, B., Revel, M., Ducassou, E., Wainer, K., Ibrahim, M., Shoaib, D., Migeon, S., Marieu,
905 V., 2011. Orbital timing of the Indian, East Asian and African boreal monsoons and the concept of a
906 “global monsoon.” *Quat. Sci. Rev.* 30, 3705–3715.
- 907 Cantalejo, B., Pickering, K. T., 2015. Orbital forcing as principal driver for fine-grained deep-marine
908 siliciclastic sedimentation, Middle-Eocene Ainsa Basin, Spanish Pyrenees. *Palaeogeography,*
909 *palaeoclimatology, palaeoecology*, 421, 24-47.
- 910 Claussen, M., Kubatzki, C., Brovkin, V., Ganopolski, A., Hoelzmann, P., & Pachur, H. J., 1999. Simulation
911 of an abrupt change in Saharan vegetation in the Mid-Holocene. *Geophysical research letters*, 26(14),
912 2037-2040.
- 913 Cochonat, P., 1998. ZAIANGO2 cruise, RV L’Atalante. doi:<http://dx.doi.org/10.17600/98010110>
- 914 Cochonat, P., 1993. GUINNESS 2 cruise, RV Le Suroît. doi: <https://doi.org/10.17600/93000190>
- 915 Cochonat, P., Robin, A., 1992. GUINNESS I cruise, RV L’Atalante. doi:<http://dx.doi.org/10.17600/92004211>
- 916 Csato, I., Granjeon, D., Catuneanu, O., Baum, G.R., 2013. A three-dimensional stratigraphic model for the
917 Messinian crisis in the Pannonian Basin , eastern Hungary 121–148. doi:10.1111/j.1365-
918 2117.2012.00553.x
- 919 Dalibard, M., Popescu, S.-M., Maley, J., Baudin, F., Melinte-Dobrinescu, M.-C., Pittet, B., Marsset, T.,
920 Dennielou, B., Droz, L., Suc, J.-P., 2014. High-resolution vegetation history of West Africa during the
921 last 145 ka. *Geobios* 47, 183–198.
- 922 deMenocal, P.B., Rind, D., 1993. Sensitivity of Asian and African climate to variations in seasonal insolation,
923 glacial ice cover, sea surface temperature, and Asian orography. *J. Geophys. Res. Atmos.* 98, 7265–
924 7287.
- 925 Deville, E., Mascle, A., Callec, Y., Huyghe, P., Lallemand, S., Lerat, O., Mathieu, X., Carillo, C.P. De,
926 Patriat, M., Pichot, T., Loubrieux, B., Granjeon, D., 2015. Tectonics and sedimentation interactions in
927 the east Caribbean subduction zone : An overview from the Orinoco delta and the Barbados
928 accretionary prism. *Mar. Pet. Geol.* 64, 76–103. doi:10.1016/j.marpetgeo.2014.12.015
- 929 Droz, L., Marsset, T., 2011. REPRESENTAI_LEG2 cruise, RV Le Suroît.
930 doi:<http://dx.doi.org/10.17600/11020020>.
- 931 Droz, L., Marsset, T., Ondras, H., Lopez, M., Savoye, B., Spy-Anderson, F.-L., 2003. Architecture of an
932 active mud-rich turbidite system: The Zaire Fan (Congo–Angola margin southeast Atlantic): Results
933 from ZaAngo 1 and 2 cruises. *Am. Assoc. Pet. Geol. Bull.* 87, 1145–1168.
- 934 Droz, L., Rigaut, F., Cochonat, P., Tofani, R., 1996. Morphology and recent evolution of the Zaire turbidite
935 system (Gulf of Guinea). *Geol. Soc. Am. Bull.* 108, 253–269.
- 936 Ducassou, E., Migeon, S., Mulder, T., Murat, A., Capotondi, L., Bernasconi, S.M., Mascle, J., 2009.
937 Evolution of the Nile deep-sea turbidite system during the Late Quaternary: influence of climate change
938 on fan sedimentation. *Sedimentology* 56, 2061–2090.

- 939 Dupont, L. (2011). Orbital scale vegetation change in Africa. *Quaternary Science Reviews*, 30(25-26), 3589-
940 3602.
- 941 Dupont, L.M., Behling, H., Jahns, S., Marret, F., Kim, J.-H., 2007. Variability in glacial and Holocene
942 marine pollen records offshore from west southern Africa. *Veg. Hist. Archaeobot.* 16, 87–100.
- 943 Dupont, L.M., Jahns, S., Marret, F., Ning, S., 2000. Vegetation change in equatorial West Africa: time-slices
944 for the last 150 ka. *Palaeogeogr. Palaeoclimatol. Palaeoecol.* 155, 95–122.
- 945 Dupont, L.M., Marret, F., Winn, K., 1998. Land-sea correlation by means of terrestrial and marine
946 palynomorphs from the equatorial East Atlantic: phasing of SE trade winds and the oceanic
947 productivity. *Palaeogeogr. Palaeoclimatol. Palaeoecol.* 142, 51–84.
- 948 Dypvik, H., Harris, N.B., 2001. Geochemical facies analysis of fine-grained siliciclastics using Th/U, Zr/Rb
949 and (Zr+ Rb)/Sr ratios. *Chem. Geol.* 181, 131–146.
- 950 Flood, R.D., Piper, D.J.W., 1997. Amazon fan sedimentation: the relationship to equatorial climate change,
951 continental denudation, and sea-level fluctuations, in: *Proceedings-ocean drilling program scientific*
952 *results*. National science foundation, pp. 653–675.
- 953 Foley, J.A., Kutzbach, J.E., Coe, M.T., Levis, S. 1994. Feedbacks between climate and boreal forests during
954 the Holocene epoch. *Nature* 371: 52-54.
- 955 Foucault, A., Powichrowski, L., Prud'homme, A., 1987. Le contrôle astronomique de la sédimentation
956 turbiditique: exemple du Flysch à Helminthoïdes des Alpes Ligures (Italie). *Comptes Rendus de*
957 *l'Académie des Sciences, Paris*, 305, 1007-1011.
- 958 Gaillardet, J., Dupré, B., Allègre, C.J., 1999. Geochemistry of large river suspended sediments: silicate
959 weathering or recycling tracer? *Geochim. Cosmochim. Acta* 63, 4037–4051.
- 960 Gaillardet, J., Dupré, B., Allègre, C.J., 1995. A global geochemical mass budget applied to the Congo Basin
961 rivers: erosion rates and continental crust composition. *Geochim. Cosmochim. Acta* 59, 3469–3485.
- 962 Galloway, W.E., 1998. Siliciclastic slope and base-of-slope depositional systems: component facies,
963 stratigraphic architecture, and classification. *Am. Assoc. Pet. Geol. Bull.* 82, 569–595.
- 964 Ganopolski, A., Kubatzki, C., Claussen, M., Brovkin, V., Petoukhov, V., 1998. The influence of vegetation-
965 atmosphere-ocean interaction on climate during the mid-Holocene. *Science*, 280(5371), 1916-1919.
- 966 Gasse, F., 2000. Hydrological changes in the African tropics since the Last Glacial Maximum. *Quat. Sci.*
967 *Rev.* 19, 189–211.
- 968 Gervais, V., Ducros, M., Granjeon, D., 2018. Probability maps of reservoir presence and sensitivity analysis
969 in stratigraphic forward modeling. *AAPG Bulletin*, 102(4), 613-628.
- 970 Gingele, F.X., Müller, P.M., Schneider, R.R., 1998. Orbital forcing of freshwater input in the Zaire Fan area
971 - clay mineral evidence from the last 200 kyr. *Palaeogeogr. Palaeoclimatol. Palaeoecol.* 138, 17–26.
- 972 Giresse, P., Wiewiora, A., Lacka, B., 1988. Mineral phases and processes within green peloids from two
973 recent 723 deposits near the Congo River mouth. *Clay Minerals* 23, 447–458.
- 974 Granjeon, D., 1997. Modelisation stratigraphique deterministe: conception et applications d'un modele
975 diffusif 3D multilithologique. PhD thesis. Université Rennes 1.

- 976 Granjeon, D., Joseph, P., 1999. Concepts and applications of a 3-D multiple lithology, diffusive model in
977 stratigraphic modeling. *SEPM Spec. Publ.* 62, 197–210.
- 978 Granjeon, D., Joseph, P., Lafont, F., Guillocheau, F., 1994. Quantification de l'eustatisme haute-fréquence et
979 de la subsidence par analyse de l'espace disponible. Application au bassin d'avant-pays sud-pyrénéen
980 (région de Jaca, Eocène). *Comptes rendus de l'Académie des sciences. Série 2*, 319(9), 1071-1077.
- 981 Groenenberg, R. M., Hodgson, D. M., Prelat, A., Luthi, S. M., Flint, S. S., 2010. Flow–deposit interaction in
982 submarine lobes: Insights from outcrop observations and realizations of a process-based numerical
983 model. *Journal of Sedimentary Research*, 80(3), 252-267.
- 984 Groenenberg, R.M., Sloff, K., Weltje, G.J., 2009. A high-resolution 2-DH numerical scheme for process-
985 based modeling of 3-D turbidite fan stratigraphy. *Comput. Geosci.* 35, 1686–1700.
- 986 Gvirtzman, Z., Csato, I., Granjeon, D., 2014. Constraining sediment transport to deep marine basins through
987 submarine channels: The Levant margin in the Late Cenozoic. *Mar. Geol.* 347, 12–26.
- 988 Hatin, T., Crosta, X., Le Hérisse, A., Droz, L., Marsset, T., 2017. Diatom response to oceanographic and
989 climatic 744 changes in the Congo fan area, equatorial Atlantic Ocean, during the last 190 ka BP.
990 *Palaeogeogr., 745 Palaeoclimato., Palaeoecol.* 469, 47-59.
- 991 Hawie, N., Marfisi, E., Saint-Ange, F., MacDonald, A. W. A., 2019. Statistical analysis of forward
992 stratigraphic models in complex salt provinces: The central Scotian Basin case study. *AAPG Bulletin*,
993 103(2), 433-467.
- 994 Hawie, N., Covault, J. A., Dunlap, D., Sylvester, Z., 2018. Slope-fan depositional architecture from high-
995 resolution forward stratigraphic models. *Marine and Petroleum Geology*, 91, 576-585.
- 996 Heard, T. G., Pickering, K. T., & Robinson, S. A., 2008. Milankovitch forcing of bioturbation intensity in
997 deep-marine thin-bedded siliciclastic turbidites. *Earth and Planetary Science Letters*, 272(1-2), 130-138.
- 998 Heezen, B.C., Menzies, R.J., Schneider, E.D., Ewing, W.M., Granelli, N.C.L., 1964. Congo submarine
999 canyon. *Am. Assoc. Pet. Geol. Bull.* 48, 1126–1149.
- 1000 Hodgson, D.M., Flint, S.S., Hodgetts, D., Drinkwater, N.J., Johannessen, E.P., Luthi, S.M., 2006.
1001 Stratigraphic evolution of fine-grained submarine fan systems, Tanqua depocenter, Karoo Basin, South
1002 Africa. *J. Sediment. Res.* 76, 20–40.
- 1003 Holtvoeth, J., Wagner, T., Horsfield, B., Schubert, C., Wand, U., 2001. Late-Quaternary supply of
1004 terrigenous organic matter to the Congo deep-sea fan (ODP site 1075): implications for equatorial
1005 African paleoclimate. *Geo-Marine Lett.* 21, 23–33.
- 1006 Hoorn, C., Guerrero, J., Sarmiento, A. S., Lorente, M. A. 1995. Andean tectonics as a cause for changing
1007 drainage pattern in Miocene northern South America. *Geology*, 23, 237-240.
- 1008 Hou, J., Wang, H., Fu, B., Zhu, L., Wang, Y., Li, Z., 2016. Effects of plant diversity on soil erosion for
1009 different vegetation patterns. *Catena* 147, 632–637.
- 1010 Jahns, S., 1996. Vegetation history and climate changes in West Equatorial Africa during the Late
1011 Pleistocene and Holocene, based on a marine pollen diagram from the Congo fan. *Veg. Hist.*
1012 *Archaeobot.* 5, 207–213.

- 1013 Jahns, S., Hüls, M., Sarnthein, M., 1998. Vegetation and climate history of west equatorial Africa based on a
 1014 marine pollen record off Liberia (site GIK 16776) covering the last 400,000 years. *Rev. Palaeobot.*
 1015 *Palynol.* 102, 277–288.
- 1016 Kane, I. A., Clare, M. A., 2019. Dispersion, accumulation and the ultimate fate of microplastics in deep-
 1017 marine environments: A review and future directions. *Frontiers in Earth Science*, 7, 80.
- 1018 Kaufman, P., Grotzinger, J.P., McCormick, D.S., 1991. Depth-dependent diffusion algorithm for simulation
 1019 of sedimentation in shallow marine depositional systems. *Kansas Geol. Surv. Bull.* 233, 489–508.
- 1020 Kettner, A. J., Syvitski, J. P., 2008. HydroTrend v. 3.0: A climate-driven hydrological transport model that
 1021 simulates discharge and sediment load leaving a river system. *Computers & Geosciences*, 34(10), 1170-
 1022 1183.
- 1023 Khripounoff, A., Vangriesheim, A., Babonneau, N., Crassous, P., Dennielou, B., Savoye, B., 2003. Direct
 1024 observation of intense turbidity current activity in the Zaire submarine valley at 4000 m water depth.
 1025 *Mar. Geol.* 194, 151–158.
- 1026 Kneller, B., 2003. The influence of flow parameters on turbidite slope channel architecture. *Marine and*
 1027 *Petroleum Geology*, 20(6-8), 901-910.
- 1028 Kolla, V., 2007. A review of sinuous channel avulsion patterns in some major deep-sea fans and factors
 1029 controlling them. *Mar. Pet. Geol.* 24, 450–469.
- 1030 Krom, M.D., Stanley, J.D., Cliff, R.A., Woodward, J.C., 2002. Nile River sediment fluctuations over the past
 1031 7000 yr and their key role in sapropel development. *Geology* 30, 71–74.
- 1032 Kutzbach, J., Bonan, G., Foley, J., Harrison, S.P., 1996. Vegetation and soil feedbacks on the response of the
 1033 African monsoon to orbital forcing in the early to middle Holocene. *Nature* 384, 623.
- 1034 Labourdette, R., Bez, M., 2010. Element migration in turbidite systems: Random or systematic depositional
 1035 processes?. *AAPG bulletin*, 94(3), 345-368.
- 1036 Lai, S.Y.J., Capart, H., 2007. Two-diffusion description of hyperpycnal deltas. *J. Geophys. Res. Earth Surf.*
 1037 112.
- 1038 Laraque, A., Bellanger, M., Adele, G., Guebanda, S., Gulemvuga, G., Pandi, A., Paturel, J.E., Robert, A.,
 1039 Tathy, J.P., Yambélé, A., 2013. Evolutions récentes des débits du Congo, de l'Oubangui et de la
 1040 Sangha. *Geo-Eco Trop* 37, 93–100.
- 1041 Laraque, A., Bricquet, J.P., Pandi, A., Olivry, J.C., 2009. A review of material transport by the Congo River
 1042 and its tributaries. *Hydrol. Process.* 23, 3216–3224.
- 1043 Laraque, A., Moukolo, N., Olivry, J.C., Bricquet, J.P., 1993. Transport en solution et en suspension par le
 1044 fleuve Congo (Zaïre) et ses principaux affluents de la rive droite. *Hydrol. Sci. J.* 38, 133–145.
- 1045 Lavier, L.L., Steckler, M.S., Brigaud, F., 2001. Climatic and tectonic control on the Cenozoic evolution of
 1046 the West African margin. *Mar. Geol.* 178, 63–80.
- 1047 Lavier, L.L., Steckler, M.S., Brigaud, F., 2000. An improved method for reconstructing the stratigraphy and
 1048 bathymetry of continental margins: Application to the Cenozoic tectonic and sedimentary history of the
 1049 Congo margin. *Am. Assoc. Pet. Geol. Bull.* 84, 923–939.

- 1050 Ledru, M., Salatino, M.L.F., Ceccantini, G., Salatino, A., Pinheiro, F., Pintaud, J., 2007. Regional assessment
1051 of the impact of climatic change on the distribution of a tropical conifer in the lowlands of South
1052 America. *Divers. Distrib.* 13, 761–771.
- 1053 Leroux, E., Rabineau, M., Aslanian, D., Granjeon, D., Droz, L., Gorini, C., 2014. Stratigraphic simulations
1054 of the shelf of the Gulf of Lions : testing subsidence rates and sea-level curves during the Pliocene and
1055 Quaternary. doi:10.1111/ter.12091
- 1056 Leroux, M., 1993. The Mobile Polar High: a new concept explaining present mechanisms of meridional air-
1057 mass and energy exchanges and global propagation of palaeoclimatic changes. *Glob. Planet. Change* 7,
1058 69–93.
- 1059 Lisiecki, L.E., Raymo, M.E., 2005. A Pliocene-Pleistocene stack of 57 globally distributed benthic $\delta^{18}O$
1060 records. *Paleoceanography* 20.
- 1061 Lopez, M., 2001. Architecture and depositional pattern of the Quaternary deep-sea fan of the Amazon. *Mar.*
1062 *Pet. Geol.*18, 479–486.
- 1063 Marret, F., Scourse, J., Jansen, J.H.F., Schneider, R., 1999. Changements climatiques et
1064 paléocéanographiques en Afrique centrale atlantique au cours de la dernière déglaciation: contribution
1065 palynologique. *Comptes Rendus l'Académie des Sci. IIA-Earth Planet. Sci.* 329, 721–726.
- 1066 Marsset, T., Droz, L., 2010. REPREZAI_LEG1 cruise, RV Pourquoi pas ?.
1067 doi:http://dx.doi.org/10.17600/10030170
- 1068 Marsset, T., Droz, L., Dennielou, B., Pichon, E., 2009. Cycles in the architecture of the Quaternary Zaire
1069 turbidite system: a possible link with climate. *Extern. Control. Deep. Depos. Syst. SEPM, Spec. Publ.*
1070 92, 89–106.
- 1071 Martins, O., Probst, J.L., 1991. Biogeochemistry of major African rivers: carbon and mineral transport, in:
1072 Degens, E., Kempe, S., Richey, J.. (Eds.), *Biogeochemical of Major World Rivers*. pp. 127–156.
- 1073 Maslin, M., Knutz, P. C., Ramsay, T. (2006). Millennial-scale sea-level control on avulsion events on the
1074 Amazon Fan. *Quaternary Science Reviews*, 25(23-24), 3338-3345.
- 1075 Michalopoulos, P., Aller, R.C., 2004. Early diagenesis of biogenic silica in the Amazon delta : Alteration,
1076 839 authigenic clay formation, and storage. *Geochimica and Cosmochimica Acta* 68, 1061-1085.
- 1077 Milliman, J. D., Syvitski, J. P., 1992. Geomorphic/tectonic control of sediment discharge to the ocean: the
1078 importance of small mountainous rivers. *The Journal of Geology*, 525-544.
- 1079 Mitchell, N.C., Huthnance, J.M., 2008. Oceanographic currents and the convexity of the uppermost
1080 continental slope. *J. Sediment. Res.* 78, 29–44.
- 1081 Moguedet, G., 1988. Les relations entre le fleuve congo et la sedimentation recente sur la marge continentale
1082 entre l'embouchure et le sud du gabon: etude hydrologique, sedimentologique et geochemique. PhD
1083 thesis, University of Angers.
- 1084 Molliex, S., Kettner, A. J., Laurent, D., Droz, L., Marsset, T., Laraque, Rabineau, M., N'Kaya, G. D. M.,
1085 2019. Simulating sediment supply from the Congo watershed over the last 155 ka. *Quaternary Science*
1086 *Reviews*, 203, 38-55.
- 1087 Mutti, E., Normark, W.R., 1987. Comparing examples of modern and ancient turbidite systems: problems
1088 and concepts, in: *Marine Clastic Sedimentology*. Springer, pp. 1–38.

- 1089 Nygard, R., Gutierrez, M., Gautam, R., Hoeg, K., 2004. Compaction behavior of argillaceous sediments as
1090 function of diagenesis. *Mar. Pet. Geol.* 21, 349–362.
- 1091 Nze Abeigne, C.R., 1997. Evolution post-rift de la marge continentale Sud-Gabon: contrôles tectonique et
1092 climatique sur la sédimentation. PhD thesis, University of Montpellier 2.
- 1093 Ortiz-Karpf, A., Hodgson, D. M., McCaffrey, W. D., 2015. The role of mass-transport complexes in
1094 controlling channel avulsion and the subsequent sediment dispersal patterns on an active margin: the
1095 Magdalena Fan, offshore Colombia. *Marine and Petroleum Geology*, 64, 58-75.
- 1096 Paola, C., Heller, P.L., Angevine, C.L., 1992. The large-scale dynamics of grain-size variation in alluvial
1097 basins, 1: Theory. *Basin Res.* 4, 73–90.
- 1098 Picot, M., Marsset, T., Droz, L., Dennielou, B., Baudin, F., Hermoso, De Rafelis, M., Sionneau, T., Cremer,
1099 M., Laurent, D., Bez, M., 2019. Monsoon control on channel avulsions in the Late Quaternary Congo
1100 Fan. *Quaternary Science Reviews*, 204, 149-171.
- 1101 Picot, M., Droz, L., Marsset, T., Dennielou, B., Bez, M., 2016. Controls on turbidite sedimentation: Insights
1102 from a quantitative approach of submarine channel and lobe architecture (Late Quaternary Congo Fan).
1103 *Mar. Pet. Geol.* 72, 423–446.
- 1104 Pirmez, C., Hiscott, R.N., Kronen, J.D., 1997. Sandy turbidite successions at the base of channel-levee
1105 systems of the Amazon Fan revealed by FMS logs and cores: unraveling the facies architecture of large
1106 submarine fans, in: *Proceedings of the Ocean Drilling Program. Scientific Results. Ocean Drilling
1107 Program*, pp. 7–33.
- 1108 Posamentier, H.W., Kolla, V., 2003. Seismic geomorphology and stratigraphy of depositional elements in
1109 deep-water settings. *J. Sediment. Res.* 73, 367–388.
- 1110 Posamentier, H.W., Erskine, R.D., Jr, R.M.M., 1991. Models for Submarine-Fan Deposition within a
1111 Sequence- Stratigraphic Framework, in: Weimer, P., Link, M.H. (Eds.), *Seismic Facies and
1112 Sedimentary Processes of Submarine Fans and Turbidite Systems*, *Frontiers in Sedimentary Geology*.
1113 Springer New York, pp. 127–136.
- 1114 Prather, B.E., Booth, J.R., Steffens, G.S., Craig, P.A., 1998. Classification, Lithologic Calibration, and
1115 Stratigraphic Succession of Seismic Facies of Intraslope Basins, Deep-Water Gulf of Mexico. *AAPG
1116 Bull.* 82, 701–728.
- 1117 Rabineau, M., Berné, S., Aslanian, D., Olivet J-L., Joseph, P., Guillocheau, F, Bourillet, J-F., Ledrezen,
1118 E., Granjeon, D., 2005: Sedimentary sequences in the Gulf of Lions: a record of 100,000 years
1119 climatic cycles, *Marine and Petroleum Geology*, 22, p. 775-804).
- 1120 Rabouille, C., Dennielou, B., Baudin, F., Raimonet, M., Droz, L., Khripounoff, A., Martinez, P., Mejanelle, L.,
1121 Michalopoulos, P., Pastor, L., Pruski, A., Ragueneau, O., Reyss, J-L., Ruffine, L., J.Schnyder, J., Stetten, E.,
1122 Taillefert, M., Tourolle, J., Olu, K., 2019. Carbon and silica megasink in deep-sea sediments of the Congo
1123 terminal lobes. *Quaternary Science Reviews*, 222, 105854.
- 1124 Reading, H.G., Richards, M., 1994. Turbidite systems in deep-water basin margins classified by grain size
1125 and feeder system. *Am. Assoc. Pet. Geol. Bull.* 78, 792–822.

- 1126 Renard, K.G., Foster, G.R., Weesies, G.A., McCool, D.K., Yoder, D.C., 1997. Predicting soil erosion by
 1127 water: a guide to conservation planning with the Revised Universal Soil Loss Equation (RUSLE). US
 1128 Government Printing Office Washington, DC.
- 1129 Sangster, C., Piper, D. J., Hawie, N., Pe-Piper, G., Saint-Ange, F., 2019. Forward stratigraphic modelling of
 1130 sediment pathways and depocentres in salt-influenced passive-margin basins: Lower Cretaceous,
 1131 central Scotian Basin. *Basin Research*, 31(4), 728-753.
- 1132 Savoye, B., 1998. ZAIANGO1 cruise, RV L'Atalante. doi:<http://dx.doi.org/10.17600/98010100>
- 1133 Savoye, B., Babonneau, N., Dennielou, B., Bez, M., 2009. Geological overview of the Angola–Congo
 1134 margin, the Congo deep-sea fan and its submarine valleys. *Deep Sea Res. Part II Top. Stud. Oceanogr.*
 1135 56, 2169–2182.
- 1136 Savoye, B., Cochonat, P., Apprioual, R., Bain, O., Baltzer, A., Bellec, V., Beuzart, P., Bourillet, J.-F., Cagna,
 1137 R., Cremer, M., 2000. Structure et évolution récente de l'éventail turbiditique du Zaïre: premiers
 1138 résultats scientifiques des missions d'exploration Zaïango1 & 2 (marge Congo–Angola). *Comptes*
 1139 *Rendus l'Académie des Sci. IIA-Earth Planet. Sci.* 331, 211–220.
- 1140 Schneider, R.R., Price, B., Müller, P.J., Kroon, D., Alexander, I., 1997. Monsoon related variations in Zaire
 1141 (Congo) sediment load and influence of fluvial silicate supply on marine productivity in the east
 1142 equatorial Atlantic during the last 200,000 years. *Paleoceanography* 12, 463–481.
- 1143 Scotchman, J. I., Pickering, K. T., Sutcliffe, C., Dakin, N., Armstrong, E., 2015. Milankovitch cyclicity
 1144 within the middle Eocene deep-marine Guaso system, Ainsa Basin, Spanish Pyrenees. *Earth-Science*
 1145 *Reviews*, 144, 107-121.
- 1146 Searđ, C., Borgomano, J., Granjeon, D., Camoin, G., 2013. Impact of environmental parameters on coral reef
 1147 development and drowning: Forward modelling of the last deglacial reefs from Tahiti (French
 1148 Polynesia; IODP Expedition# 310). *Sedimentology* 60, 1357–1388.
- 1149 Sionneau, T., Droz, L., Marsset, T., Dennielou, B., Bez, M., 2010. Congo-Zaire detrital supply variability
 1150 during the last 200 ka: a possible explanation for the longitudinal migration of the Zaire fan
 1151 depocenters. *International Sedimentological Congress, 2010, Mendoza (Argentina)*.
- 1152 Sømme, T.O., Helland-Hansen, W., Martinsen, O.J., Thurmond, J.B., 2009. Relationships between
 1153 morphological and sedimentological parameters in source-to-sink systems: a basis for predicting semi-
 1154 quantitative characteristics in subsurface systems. *Basin Res.* 21, 361–387.
- 1155 Spratt, R. M., Lisiecki, L. E. (2016). A Late Pleistocene sea level stack. *Climate of the Past*, 12(4), 1079-
 1156 1092.
- 1157 Steckler, M.S., Mountain, G.S., Miller, K.G., Christie-Blick, N., 1999. Reconstruction of Tertiary
 1158 progradation and clinoform development on the New Jersey passive margin by 2-D backstripping. *Mar.*
 1159 *Geol.* 154, 399–420.
- 1160 Stouthamer, E., Berendsen, H. J., 2007. Avulsion: the relative roles of autogenic and allogenic processes.
 1161 *Sedimentary Geology*, 198(3-4), 309-325.
- 1162 Summerfield, M.A., Hulton, N.J., 1994. Natural controls of fluvial denudation rates in major world drainage
 1163 basins. *J. Geophys. Res. Ser.* 99, 13–871.

- 1164 Syvitski, J.P.M., Milliman, J.D., 2007. Geology, geography, and humans battle for dominance over the
1165 delivery of fluvial sediment to the coastal ocean. *J. Geol.* 115, 1–19.
- 1166 Syvitski, J.P.M., Peckham, S.D., Hilberman, R., Mulder, T., 2003. Predicting the terrestrial flux of sediment
1167 to the global ocean: a planetary perspective. *Sediment. Geol.* 162, 5–24.
- 1168 Syvitski, J. P., Morehead, M. D., Nicholson, M., 1998. HYDROTREND: a climate-driven hydrologic-
1169 transport model for predicting discharge and sediment load to lakes or oceans. *Computers &*
1170 *Geosciences*, 24(1), 51-68.
- 1171 Toucanne, S., Zaragosi, S., Bourillet, J. F., Dennielou, B., Jorry, S. J., Jouet, G., & Cremer, M., 2012.
1172 External controls on turbidite sedimentation on the glacially-influenced Armorican margin (Bay of
1173 Biscay, western European margin). *Marine Geology*, 303, 137-153.
- 1174 Toucanne, S., Zaragosi, S., Bourillet, J. F., Naughton, F., Cremer, M., Eynaud, F., Dennielou, B., 2008.
1175 Activity of the turbidite levees of the Celtic–Armorican margin (Bay of Biscay) during the last 30,000
1176 years: imprints of the last European deglaciation and Heinrich events. *Marine Geology*, 247(1-2), 84-
1177 103.
- 1178 Turakiewicz, G., 2004. Les mécanismes forçants dans les éventails turbiditiques de marges matures: exemple
1179 de l'éventail quaternaire du Congo. PhD thesis, University of Montpellier 2.
- 1180 Van Weering, T.C.E., Van Iperen, J., 1984. Fine-grained sediments of the Zaire deep-sea fan, southern
1181 Atlantic Ocean. *Geol. Soc. London, Spec. Publ.* 15, 95–113.
- 1182 Weber, M.E., Wiedicke-Hombach, M., Kudrass, H.R., Erlenkeuser, H., 2003. Bengal Fan sediment transport
1183 activity and response to climate forcing inferred from sediment physical properties. *Sediment. Geol.*
1184 155, 361–381.
- 1185 Wefer, G., Berger, W.H., Richter, C., 1998. Facies patterns and authigenic minerals of upwelling deposits off
1186 Southwest Africa, in: *Proceedings of the Ocean Drilling Program. Initial Reports. Ocean Drilling*
1187 *Program*, pp. 487–504.
- 1188 Weldeab, S., Lea, D.W., Schneider, R.R., Andersen, N., 2007. 155,000 years of West African monsoon and
1189 ocean thermal evolution. *Science* (80). 316, 1303–1307.
- 1190 Weltje, G., de Boer, P. L., 1993. Astronomically induced paleoclimatic oscillations reflected in Pliocene
1191 turbidite deposits on Corfu (Greece): implications for the interpretation of higher order cyclicality in
1192 ancient turbidite systems. *Geology*, 21(4), 307-310.
- 1193 Zabel, M., Schneider, R.R., Wagner, T., Adegbe, A.T., de Vries, U., Kolonic, S., 2001. Late Quaternary
1194 climate changes in Central Africa as inferred from terrigenous input to the Niger Fan. *Quat. Res.* 56,
1195 207–217.
- 1196 Zhou, P., Luukkanen, O., Tokola, T., Nieminen, J., 2008. Effect of vegetation cover on soil erosion in a
1197 mountainous watershed. *Catena* 75, 319–325.
- 1198

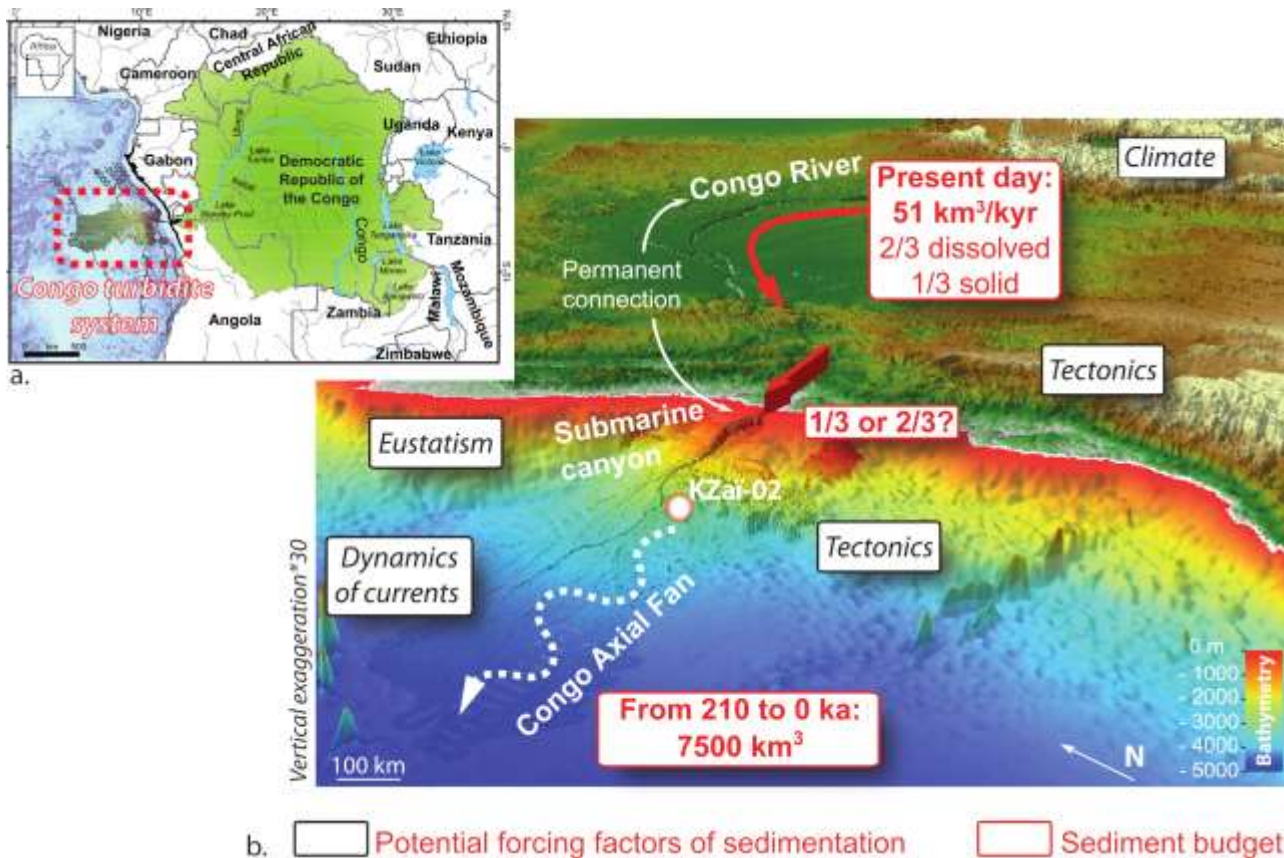
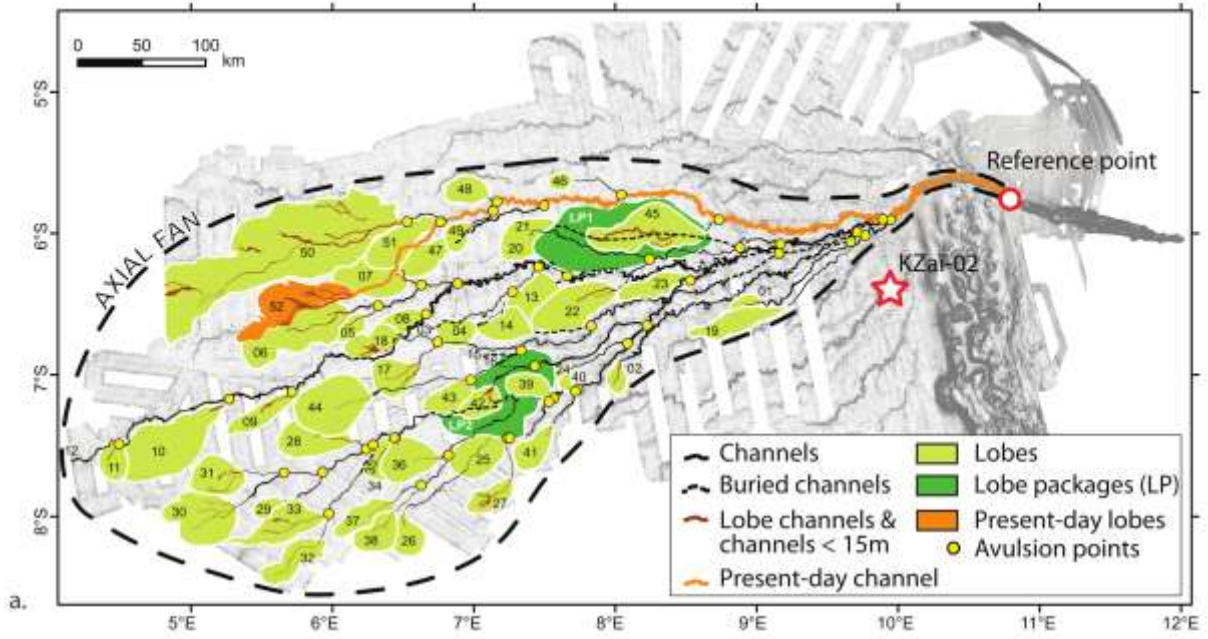
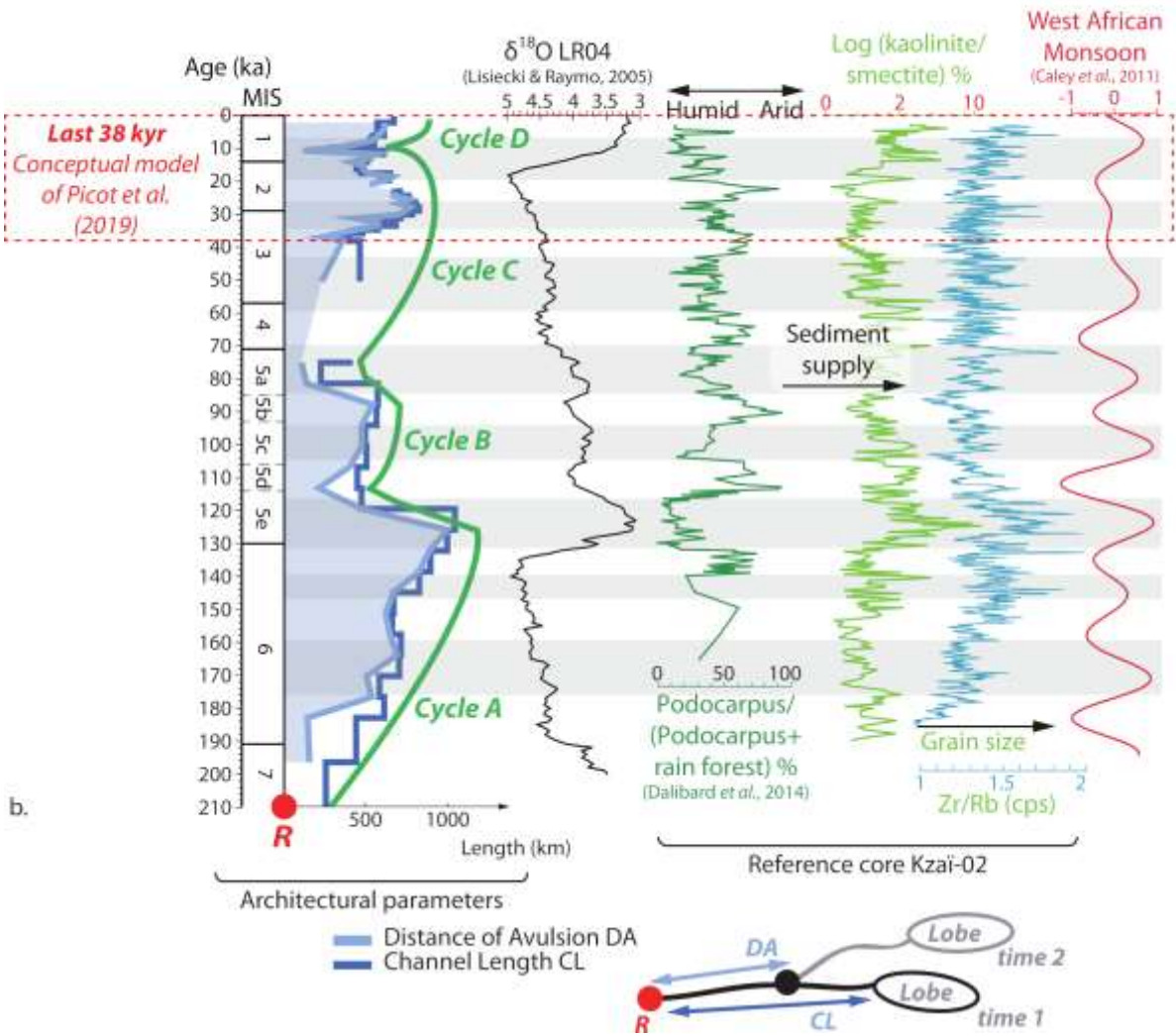


Figure 1



a.



b.

Figure 2

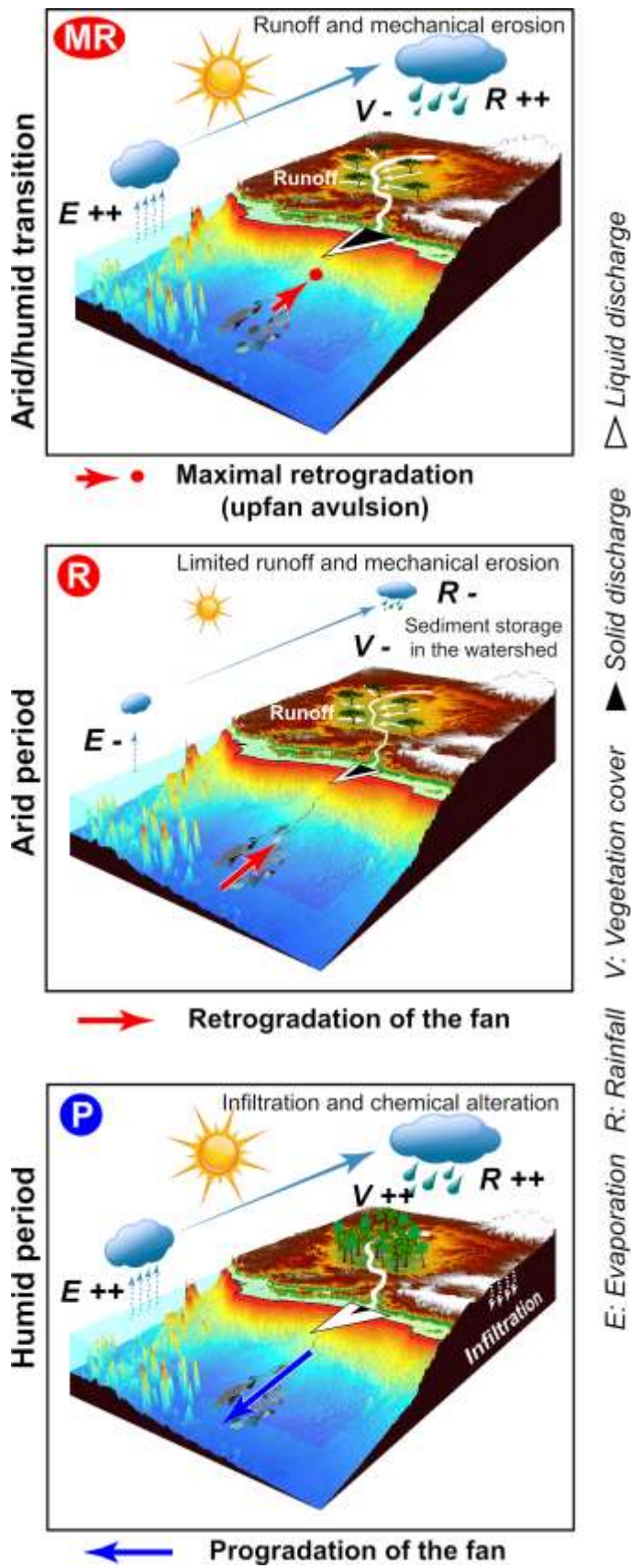


Figure 3

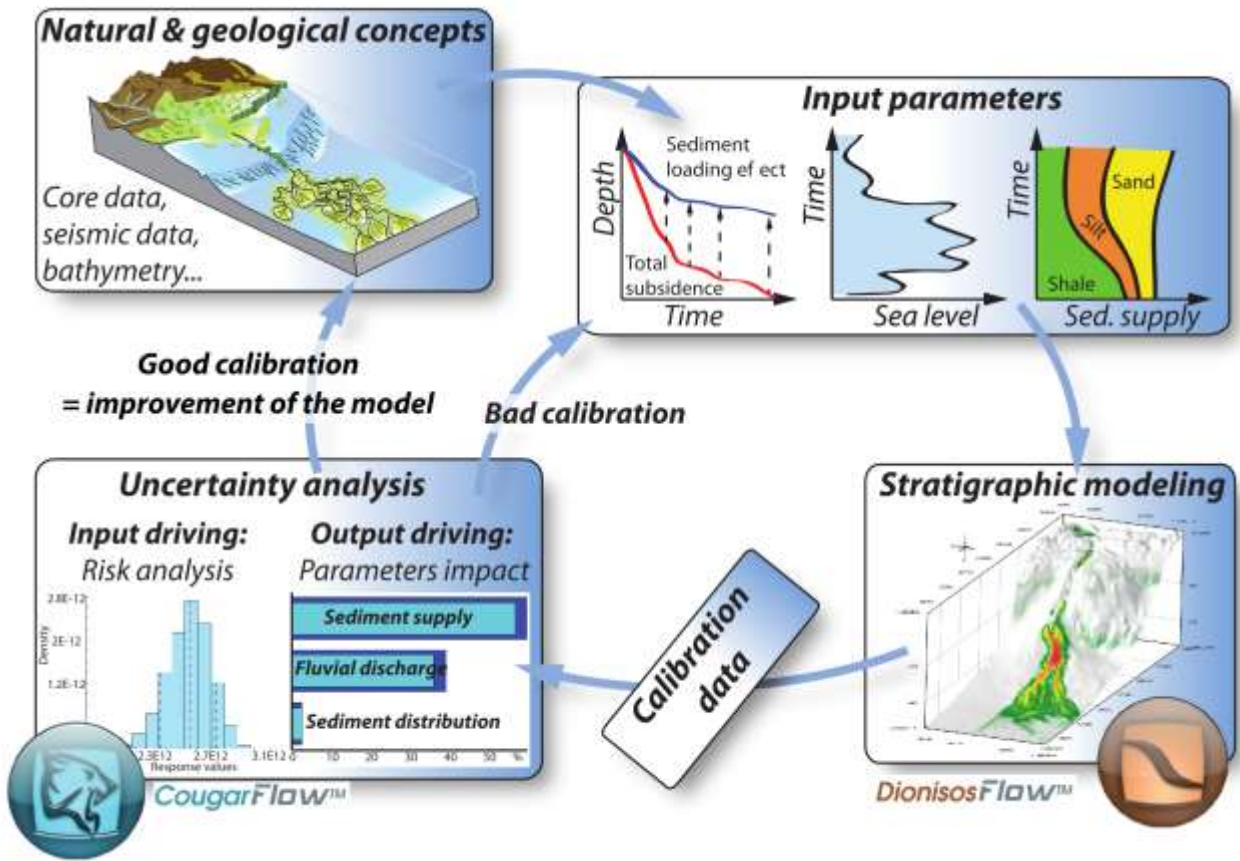
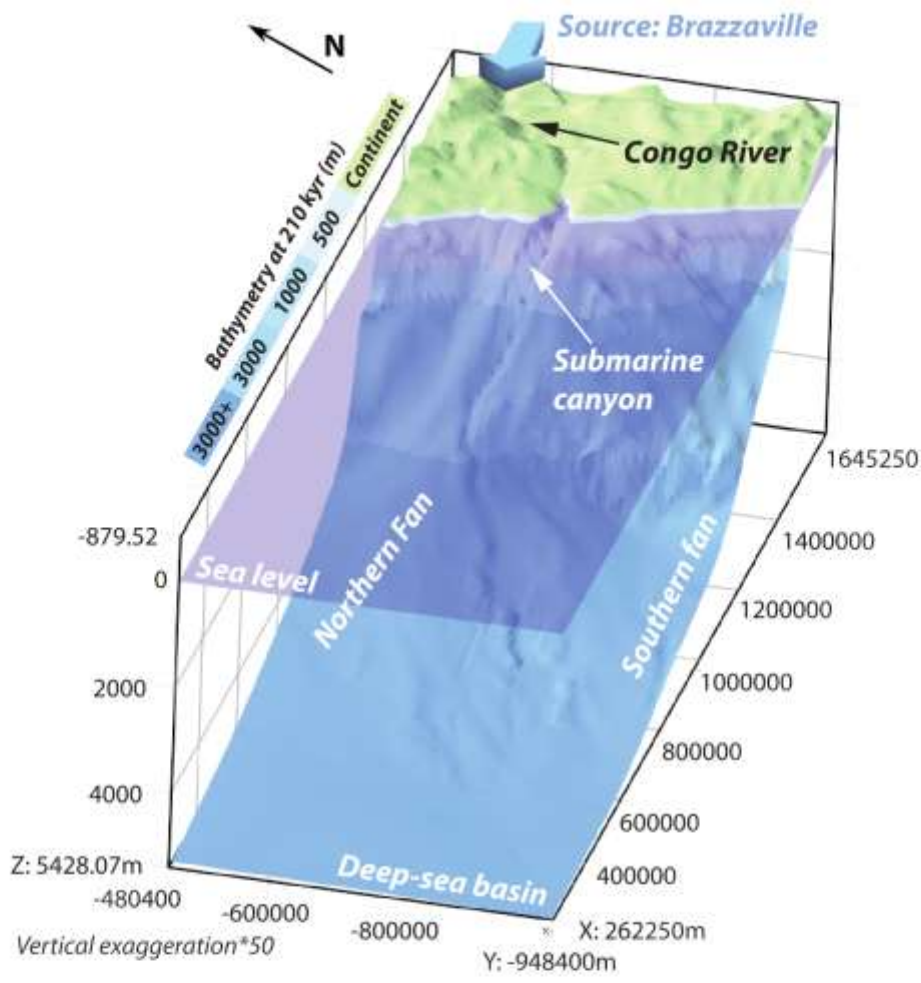


Figure 4



Model characteristics

Display time: from 210 to 0 ka
 Time step: 5 kyr
 Model size: 1383*468 km²
 Cell dimension: 6*6 km²
 Model boundaries: closed

Source characteristics

	Qw (.10 ³ m ³ /s):	Qs (.10 ³ km ³ /Myr):
Mean	41	37
Glacial periods	Between 18 & 65	Between 24 & 46
Interglacial periods	Between 32 & 62	

Lithologies: sand and mud (compaction laws by default)

Sand/(sand+mud) - Glacial periods: 24%
 Interglacial periods: 30%

Sea level variation: LR04 (Spratt and Lisiecki, 2016)

No subsidence

Diffusion coefficients K (constant over time)

	Sand	Mud
Gravity-driven K_{gravity}		
Continental (km ² /kyr)	0.001	0.001
Marine (km ² /kyr)	0.01	0.01
Water-driven K_{water}		
Continental (km ² /kyr)	100	100
Marine (km ² /kyr)	1.5	10
High-energy short-term: K_{hest}		
Continental (km ² /kyr)	100	100
Marine (km ² /kyr)	1.5	10

Figure 5

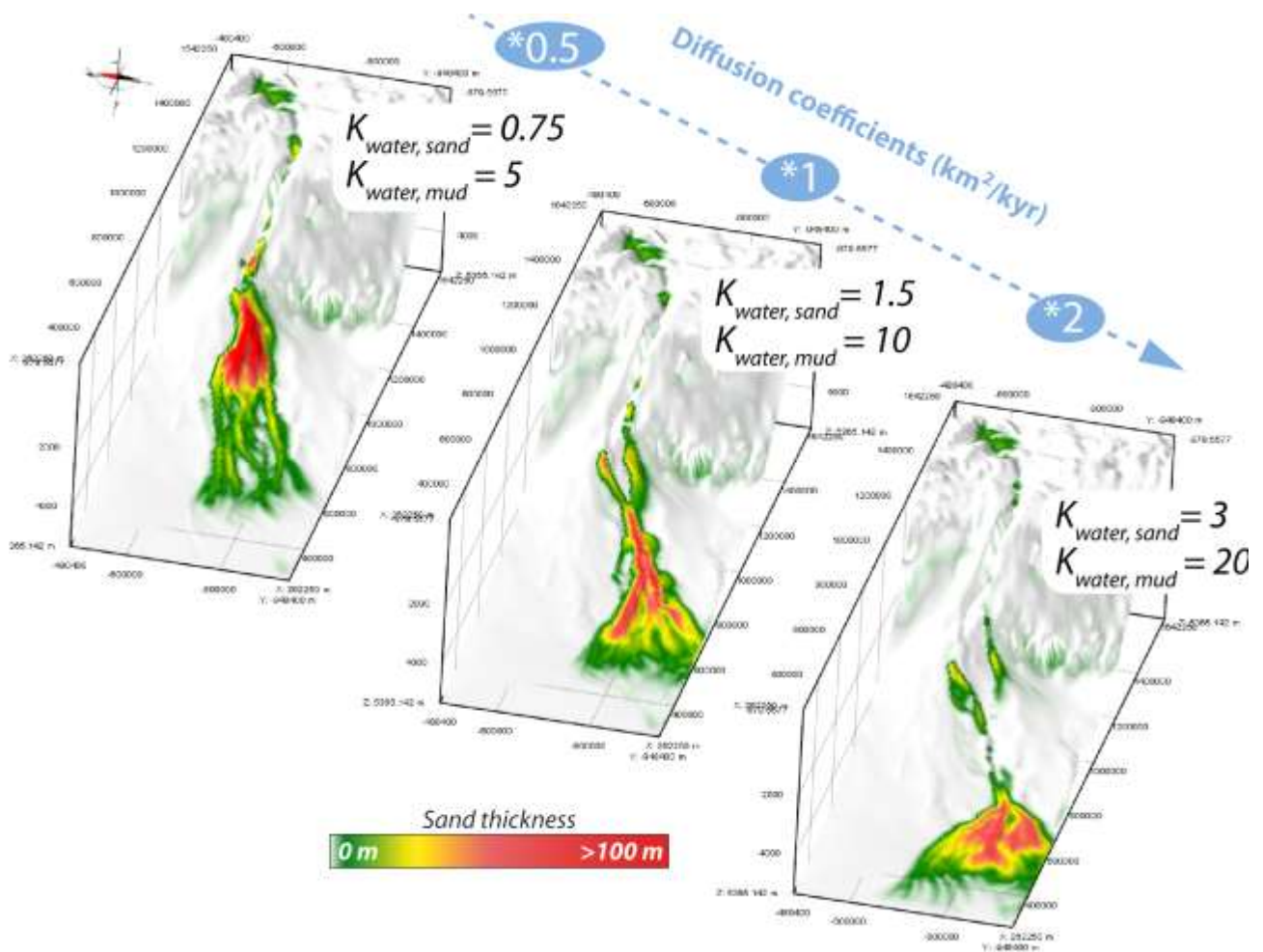


Figure 6

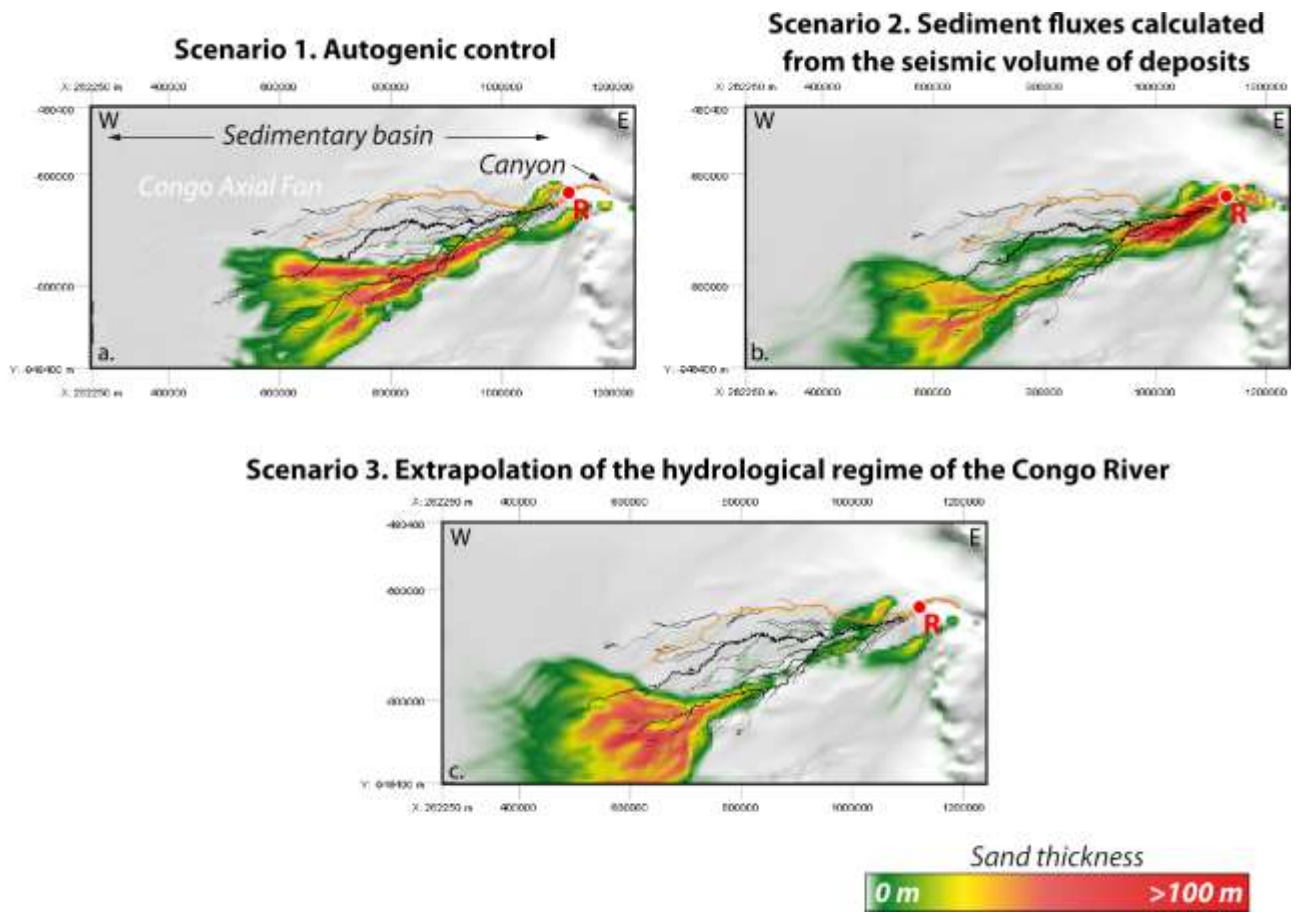
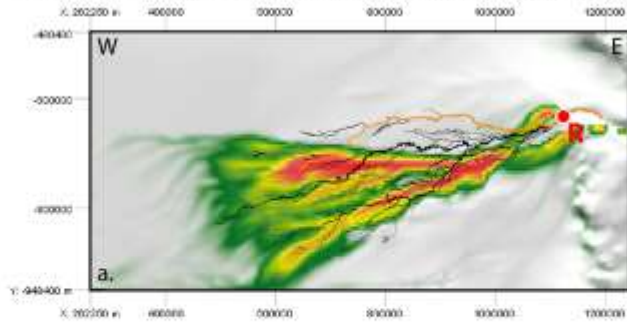
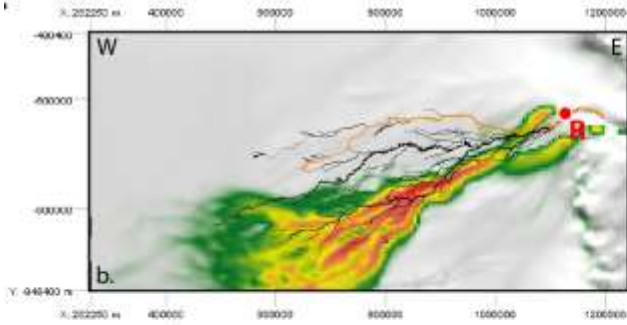


Figure 7

Scenario 4a. West African Monsoon (Caley et al., 2011)



Scenario 4b. Precession cycle - sinusoid



Scenario 4c. Precession cycle - sinusoid+sawtooth

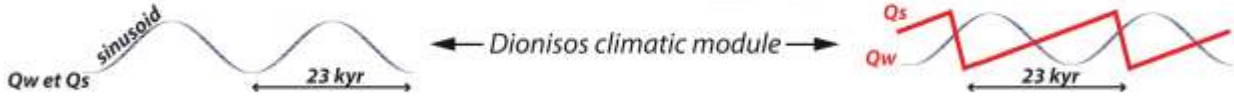
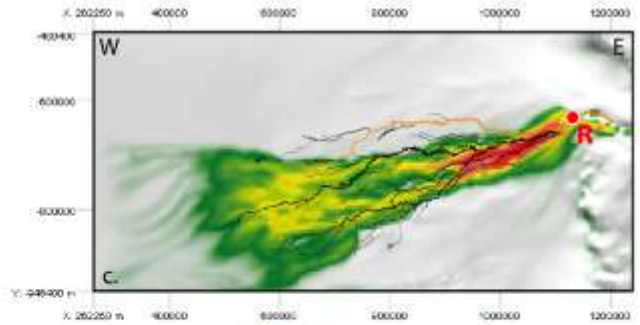
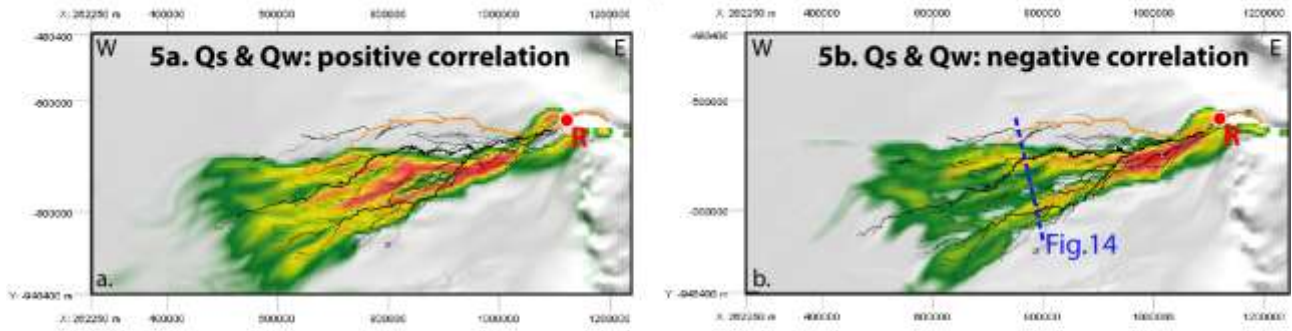


Figure 8

**Scenario 5. Marine proxy of vegetation cover changes in the watershed
Podocarpus/(Podocarpus+rainforest) - KZai-02**



**Scenario 6. Marine proxy of the timing of fluvial discharge
Kaolinite/Smectite - KZai-02**

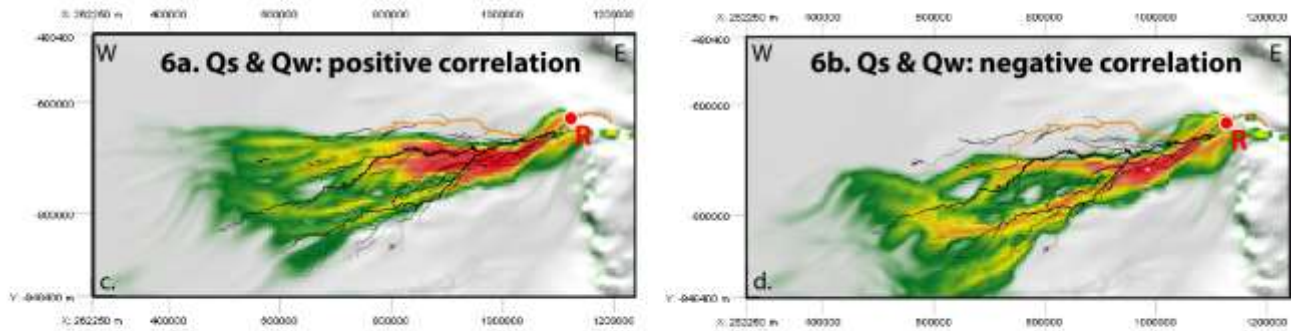


Figure 9

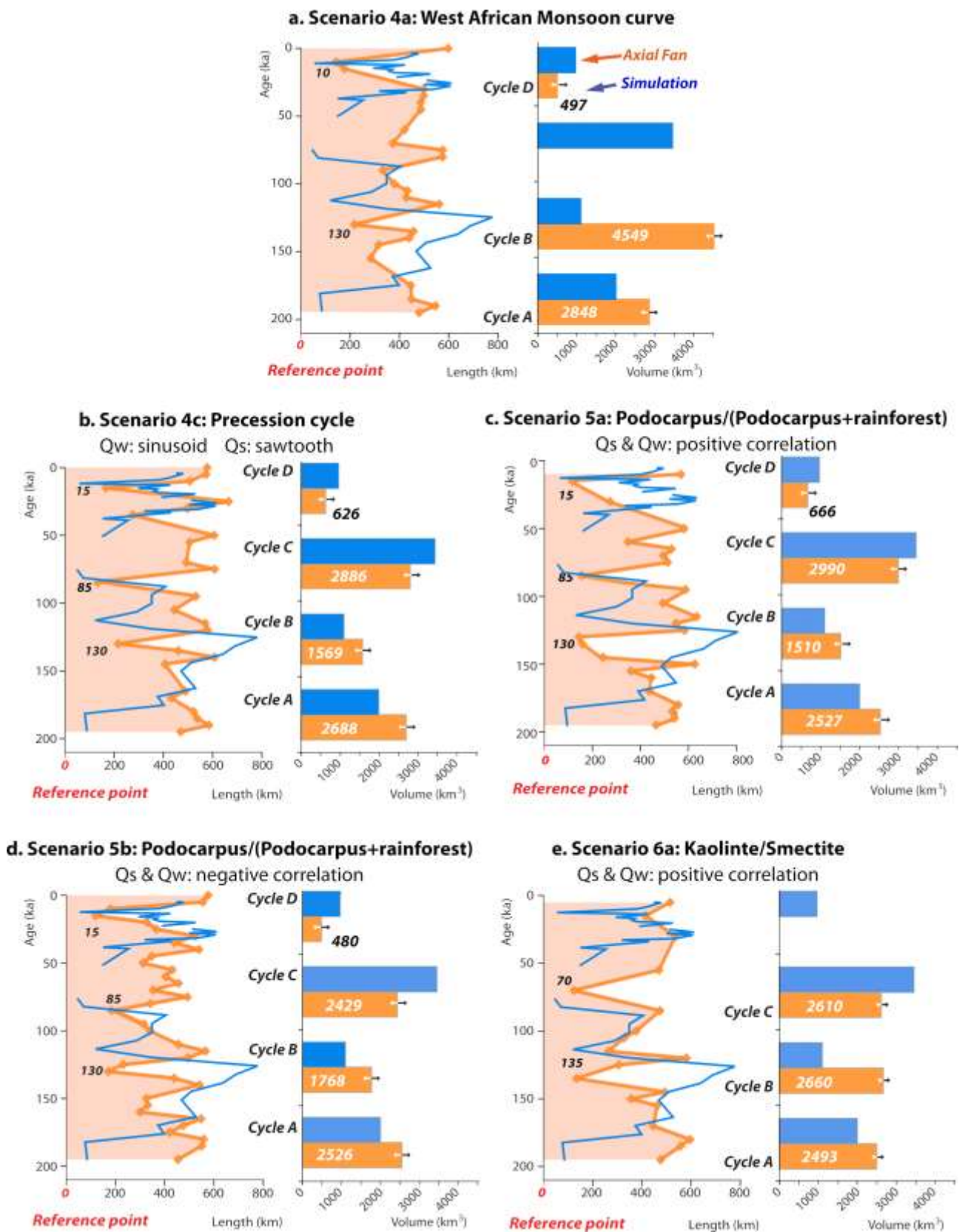


Figure 10

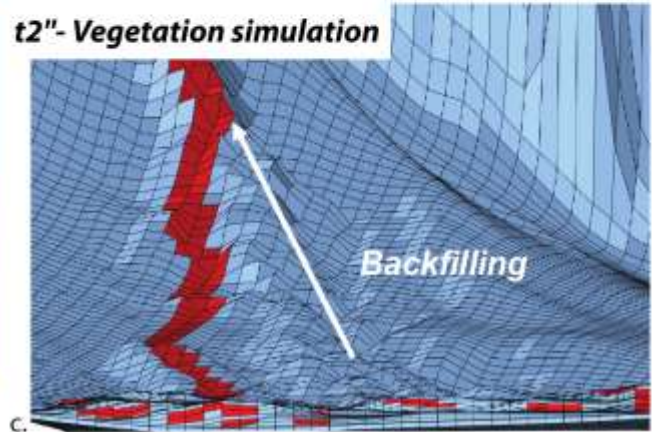
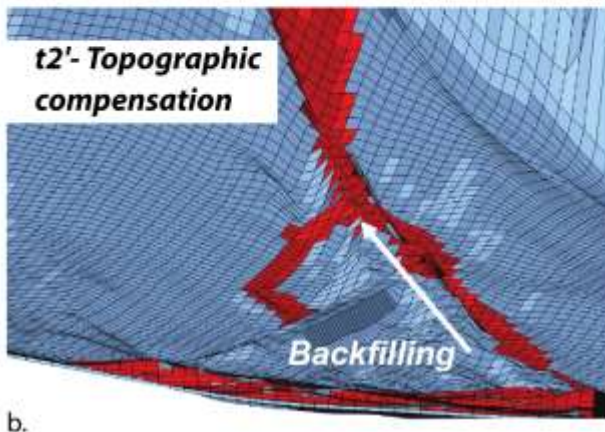
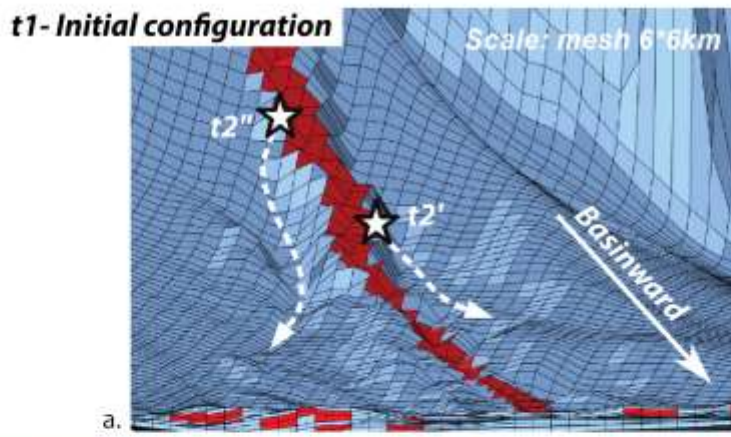


Figure 11

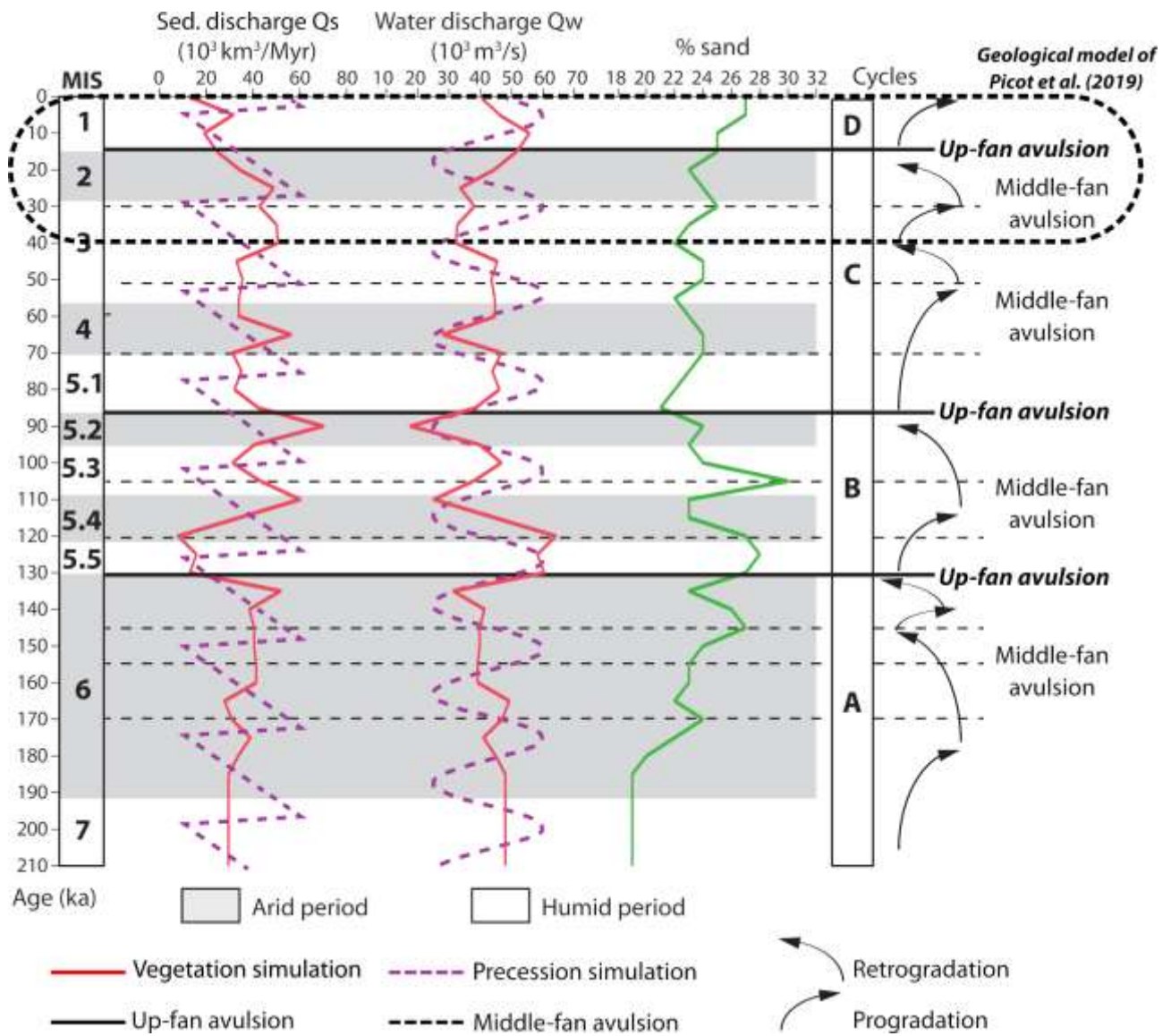


Figure 12

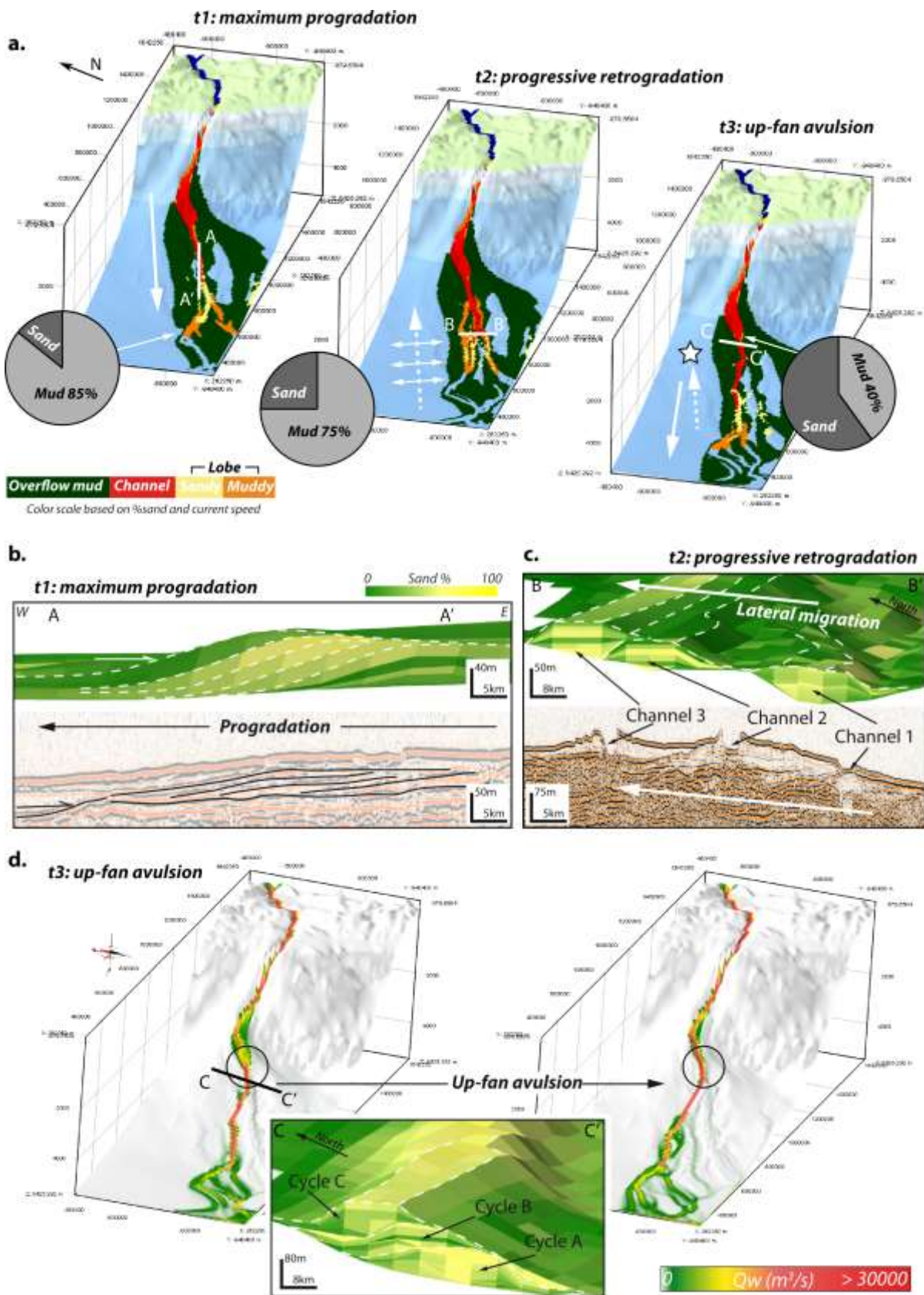


Figure 13

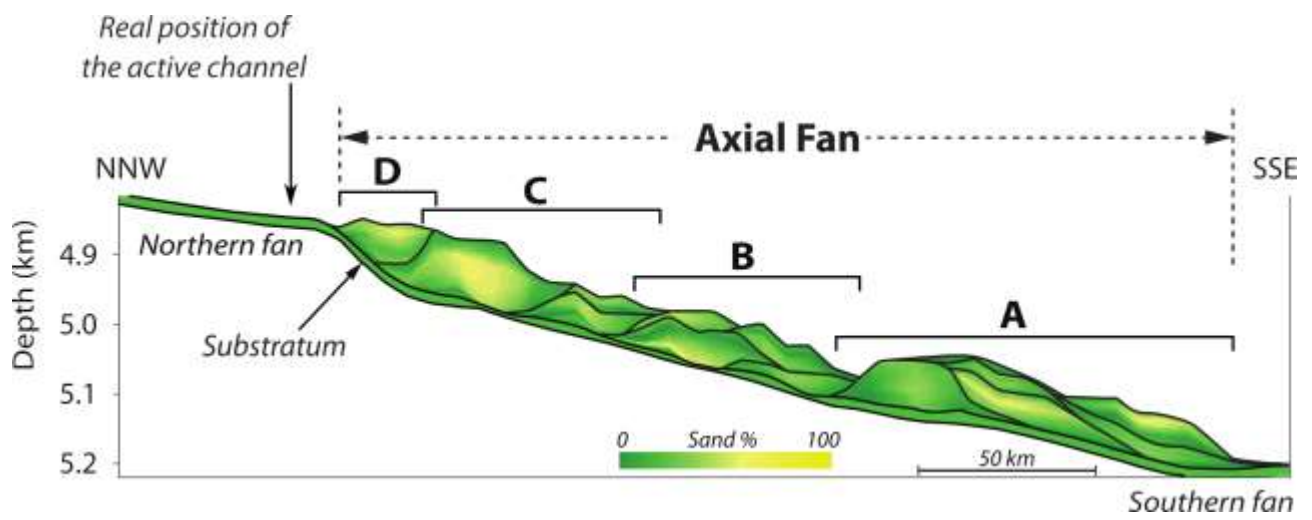


Figure 14